

1  
2  
3  
4  
5  
6  
7  
8  
9  
10  
11  
12  
13  
14  
15  
16  
17  
18  
19  
20  
21  
22  
23  
24  
25  
26  
27  
28  
29  
30  
31  
32  
33  
34  
35  
36  
37  
38  
39  
40  
41  
42  
43  
44  
45  
46  
47  
48  
49  
50  
51  
52  
53  
54  
55  
56  
57  
58  
59  
60  
61  
62  
63  
64  
65

1 **Geochemical constraints on basalt petrogenesis in the Strait of Sicily Rift Zone (Italy):**  
2 **Insights into the importance of short lengthscale mantle heterogeneity.**

3 Submitted to *Chemical Geology*

4 John Charles White<sup>1,\*</sup>, David A. Neave<sup>2</sup>, Silvio G. Rotolo<sup>3,4</sup>, and Don F. Parker<sup>5,†</sup>.

5 <sup>1</sup>Department of Geosciences  
6 Eastern Kentucky University  
7 521 Lancaster Ave., Science 2234  
8 Richmond, KY 40475 USA

9  
10 <sup>2</sup>Department of Earth and Environmental Sciences  
11 The University of Manchester  
12 Oxford Road, Manchester  
13 M13 9PL, UNITED KINGDOM

14  
15 <sup>3</sup>Dipartimento di Scienze della Terra e del Mare (DiSTeM)  
16 Università di Palermo  
17 Via Archirafi 36  
18 90123 Palermo ITALY

19  
20 <sup>4</sup>Istituto Nazionale di Geofisica e Vulcanologia (INGV)  
21 Sezione di Palermo  
22 Via Ugo La Malfa 153  
23 90146 Palermo ITALY

24  
25 <sup>5</sup>Department of Geosciences  
26 Baylor University  
27 Waco, TX 76798 USA

28  
29 \*Corresponding author: john.white@eku.edu (e-mail), +1 859-622-1276 (phone), +1 859-622-  
30 3357 (fax).

31  
32 † Present address: School of Math and Science, Wayland Baptist University, 1900 West 7<sup>th</sup>  
33 Street, Plainview, TX 79072 USA

1  
2  
3  
4 **35 Abstract**

5  
6 **36** Igneous activity from the late Miocene to historic time (most recently 1891 CE) in the Strait of  
7  
8  
9 **37** Sicily has created two volcanic islands (Pantelleria and Linosa) and several seamounts. These  
10  
11 **38** volcanoes are dominated by transitional (ol+hy-normative) to alkaline (ne-normative) basaltic  
12  
13  
14 **39** lavas and scoriae; volcanic felsic rocks (peralkaline trachyte-rhyolite) crop out only on  
15  
16 **40** Pantelleria. Although most likely erupted through continental crust, basalts demonstrate no  
17  
18  
19 **41** evidence of crustal contamination and are geochemically similar to oceanic island basalts (OIB).  
20  
21 **42** Despite their isotopic similarities, there are considerable compositional differences with respect  
22  
23  
24 **43** to major and trace element geochemistry both between and within the two islands that are due to  
25  
26 **44** short-length scale mantle heterogeneity beneath the region as well as variability in partial  
27  
28  
29 **45** melting and magma storage conditions. Published geophysical surveys suggest that lithospheric  
30  
31 **46** thickness beneath both islands is ~60 km; this is consistent with the results of our geochemical  
32  
33  
34 **47** modelling (59-60 km), which also suggest mantle potential temperatures between 1415-1435°C,  
35  
36 **48** similar to those documented in other continental passive rifts. Trace element and isotopic data  
37  
38  
39 **49** reveal that the asthenosphere beneath the Strait of Sicily is heterogenous at both inter-island  
40  
41 **50** (100s of km) and intra-island (10s of km) scales. Although there is some compositional overlap  
42  
43  
44 **51** between the two major synthemms at Linosa, in general the older magmas (Arena Bianca, 700 ka)  
45  
46 **52** formed as a result of ~5% partial melting of a depleted MORB mantle (DMM) source enriched  
47  
48  
49 **53** with a relatively small amount of recycled MORB material, whereas the younger magmas  
50  
51 **54** (Monte Bandiera, 530 ka) formed as a result of ~2% partial melting of a similar mantle source.  
52  
53 **55** Pantelleria magmas formed from a higher degree (~6%) of partial melting of a DMM source  
54  
55 **56** with a relatively greater amount of recycled MORB material and possibly other components.  
56  
57 **57** Geochemical modelling also suggests the older magmas on Linosa differentiated at a much  
58  
59  
60  
61  
62  
63  
64  
65

1  
2  
3  
4 58 shallower level (~8 km) than the younger magmas (~25 km, at or below the base of the crust)  
5  
6 59 prior to eruption. Magmas stored in higher-level reservoirs were effectively homogenized and  
7  
8  
9 60 preserve a narrower compositional range than magmas sourced from depth. Data for the  
10  
11 61 seamounts are scarce and compromised by significant seawater alteration; thus, these volcanic  
12  
13  
14 62 centers cannot be modelled but based on comparative geochemistry with the islands are likely  
15  
16 63 the result of even smaller (<2%) degrees of partial melting beneath thicker (>60 km) lithosphere.  
17  
18  
19 64 Despite the geophysical similarities between the two islands in terms of lithospheric thickness  
20  
21 65 and crustal thinning, melt productivity has been greater at Pantelleria, producing a much larger  
22  
23  
24 66 island and sustaining felsic magmatism, which we hypothesize may ultimately be entirely due to  
25  
26 67 the local occurrence of much more fusible mantle.  
27  
28

29 68  
30  
31 69 **Keywords:** Strait of Sicily Rift Zone, Continental-OIB, Alkali Basalt, Mantle Melting, Mantle  
32  
33 70 Heterogeneity  
34  
35  
36 71  
37

## 38 72 **1. Introduction**

39  
40  
41 73 The Mediterranean Sea between the island of Sicily and the Tunisian coast is the setting  
42  
43 74 for magmatism with an Oceanic Island Basalt (OIB)-like affinity that has produced two islands  
44  
45 75 (Pantelleria and Linosa) and several seamounts that occur subparallel to the faulted margins of  
46  
47  
48 76 two of the three northwest-southeast trending grabens that comprise the Strait of Sicily Rift Zone  
49  
50  
51 77 (SSRZ; Figure 1). Transitional (hy+ol-normative) to alkali (ne-normative) basaltic lavas and  
52  
53 78 tuffs occur throughout the SSRZ, with evolved lavas and tuffs (peralkaline trachyte and rhyolite  
54  
55 79 [pantellerite]) cropping out only at Pantelleria, where they form a bimodal association typical of  
56  
57  
58 80 intraplate magmatic settings (Mahood and Hildreth, 1986; Civetta et al., 1998; Bindi et al., 2002;  
59  
60  
61  
62  
63  
64  
65

1  
2  
3  
4 81 Rotolo et al., 2006; Di Bella et al., 2008; White et al., 2009; Neave et al., 2012; Avanzinelli et  
5  
6  
7 82 al., 2014).

8  
9 83 Geochemical studies have revealed that the mantle source for the SSRZ is almost  
10  
11 84 isotopically homogenous: basalts throughout the rift zone have nearly identical  $^{87}\text{Sr}/^{86}\text{Sr}$  ratios  
12  
13 85 (Linosa:  $0.7031 \pm 0.0001$ ; Pantelleria:  $0.7032 \pm 0.0001$ ; Seamounts:  $0.7035 \pm 0.0005$ ) and very  
14  
15  
16 86 similar  $^{143}\text{Nd}/^{144}\text{Nd}$  ratios (Linosa:  $0.51291\text{-}0.51297$  [ $\epsilon_{\text{Nd}} = 5.9 \pm 0.5$ ]; Pantelleria:  $0.51287\text{-}$   
17  
18  
19 87  $0.51299$  [ $\epsilon_{\text{Nd}} = 6.3 \pm 0.5$ ]; Seamounts:  $0.51299\text{-}0.51312$  [ $\epsilon_{\text{Nd}} = 7.7 \pm 0.5$ ]) (Esperança and Crisci,  
20  
21  
22 88 1995; Civetta et al., 1998; Rotolo et al., 2006; Di Bella et al., 2008; Avanzinelli et al., 2014).

23  
24 89 Helium isotopes recorded at both Pantelleria and Linosa are also similar ( $^3\text{He}/^4\text{He} = 7.3\text{-}7.6$   
25  
26 90  $\text{R}/\text{R}_a$ ; Parello et al., 2000; Fouré et al., 2012) and MORB-like ( $8 \pm 1 \text{ R}/\text{R}_a$ ; Class and Goldstein,  
27  
28  
29 91 2005). Intra- and inter-island lead isotope ratio variations are larger, becoming more radiogenic

30  
31 92 from the older Linosa suite (1070 to 530 ka;  $^{206}\text{Pb}/^{204}\text{Pb} = 19.320\text{-}19.540$ ) to the paleo-

32  
33  
34 93 Pantelleria suite (120-80 ka;  $^{206}\text{Pb}/^{204}\text{Pb} = 19.664\text{-}19.981$ ), with the younger (29-10 ka) neo-

35  
36 94 Pantelleria suite showing intermediate values ( $^{206}\text{Pb}/^{204}\text{Pb} = 19.445\text{-}19.791$ ; Avanzinelli et al.,

37  
38  
39 95 2014) and the Seamounts having a range that overlaps all of these ( $^{206}\text{Pb}/^{204}\text{Pb} = 19.153\text{-}19.693$ ;

40  
41 96 Rotolo et al., 2006). These isotopic data place the Pantelleria and Linosa basalts on the Sr-Nd

42  
43 97 mantle array between depleted MORB mantle (DMM) and primitive mantle (PM), where they

44  
45  
46 98 plot with OIB. On Sr-Nd-Pb diagrams they plot in the compositional space assigned to

47  
48  
49 99 “Prevalent Mantle” (PREMA) (Zindler and Hart, 1986; Stracke, 2012). These results have been

50  
51 100 used to support diverse interpretations for the source origin of basaltic magmatism in the SSRZ:

52  
53 101 (1) lithospheric mantle chemically modified by the addition of recycled MORB material

54  
55  
56 102 (Esperança and Crisci, 1995); (2) depleted MORB mantle enriched by a fossil plume of deep

57  
58 103 mantle material (Civetta et al., 1998; Rotolo et al., 2006); (3) a mixture of asthenospheric and

1  
2  
3  
4 104 metasomatized lithospheric mantle (Di Bella et al., 2008); and (4) asthenosphere enriched with  
5  
6  
7 105 an eclogitic component representing recycled MORB material (Avanzinelli et al., 2014). In this  
8  
9 106 latter study, Avanzinelli et al. (2014) included the results of U-series disequilibrium systematics  
10  
11 107 for the neo-Pantelleria lavas and concluded that the sources for these are strictly asthenospheric  
12  
13  
14 108 with no need for interaction with lithospheric mantle or continental crust nor any need for a  
15  
16 109 metasomatic component, thus ruling out hypotheses (1) and (3) listed above.

17  
18  
19 110 Unlike their isotopic ratios, the major and trace element geochemistry of the basalts  
20  
21 111 demonstrates considerable variability. At Pantelleria, Civetta et al. (1998) divided the basalts into  
22  
23 112 “High Ti-P” and “Low Ti-P” types, with the former also characterized by higher concentrations  
24  
25  
26 113 of incompatible trace elements and higher LREE/HREE than the latter, which they attributed to  
27  
28  
29 114 different degrees of partial melting from a locally heterogeneous asthenospheric mantle (cf.  
30  
31 115 Mahood and Baker, 1986). Similar differences were described on Linosa, where Di Bella et al.  
32  
33 116 (2008) recognized a “Trend-A” and “Trend-B”, with the former having higher  $K_2O$ ,  $P_2O_5$ ,  
34  
35  
36 117 incompatible trace elements (e.g., Rb, Th), and LREE/HREE at a given MgO. Although Di Bella  
37  
38 118 et al. (2008) attributed the differences between the volcanic centers of the SSRZ to varying  
39  
40  
41 119 degrees of partial melting from heterogeneous mantle sources, they modelled the Linosa trends  
42  
43 120 as differentiates from a common primary magma (their hypothetical “Trend-C”).

44  
45 121 Several methods have been proposed to constrain mantle source compositions and partial  
46  
47  
48 122 melting parameters using major and trace element geochemistry. The first goal of this paper is to  
49  
50  
51 123 compare the results of some of these methods, including: (1) the use of olivine-liquid  
52  
53 124 geothermobarometry to determine the average depth of partial melting and temperature of melt  
54  
55 125 segregation from calculated primary basalts (Lee et al., 2009); (2) the use of major- and trace-  
56  
57  
58 126 element ratios to constrain mantle sources (e.g., Jackson and Dasgupta, 2008; Stracke and  
59  
60  
61  
62  
63  
64  
65

1  
2  
3  
4  
5  
6  
7  
8  
9  
10  
11  
12  
13  
14  
15  
16  
17  
18  
19  
20  
21  
22  
23  
24  
25  
26  
27  
28  
29  
30  
31  
32  
33  
34  
35  
36  
37  
38  
39  
40  
41  
42  
43  
44  
45  
46  
47  
48  
49  
50  
51  
52  
53  
54  
55  
56  
57  
58  
59  
60  
61  
62  
63  
64  
65

127 Bourdon, 2009; Dasgupta et al., 2010; Davis et al., 2013; Yang and Zhou, 2013); and (3) rare  
128 earth element (REE) inverse models using the INVMEL algorithm to constrain mantle source  
129 composition and the degree and depth range of partial melting (McKenzie and O’Nions, 1991,  
130 1995). The second goal of this paper is to use the results of these various geochemical models  
131 to: (1) determine the conditions of partial melting in the asthenosphere beneath the SSRZ; (2)  
132 discriminate between the effects of lithospheric thickness, source lithology, and magma storage  
133 on the geochemistry of these basalts; and (3) constrain the magma storage conditions in the crust  
134 and describe its effect on basalt geochemistry.

**2. Geologic setting**

137 The SSRZ is a northwest-southeast trending transtensional rift system situated on the  
138 Pelagian Block, the northern promontory of the African plate that represents the foreland domain  
139 of the Apennine-Sicilian-Maghrebian orogen (Catalano et al., 2009; Martinelli et al., 2019). The  
140 SSRZ consists of three basins: the Pantelleria Trough, the Linosa Trough, and the Malta Trough.  
141 Water depth is <400 m beneath most of the Pelagian Block, increasing to ~1350 m in the  
142 Pantelleria Trough, ~1580 m in the Linosa Trough, and ~1720 m in the Malta Trough (Calanchi  
143 et al., 1989; Civile et al., 2010). Volcanoes are present in or adjacent to all except the Malta  
144 Trough, and include two islands (Pantelleria and Linosa) and several seamounts. The thickness  
145 of the crust throughout most of the Pelagian Block is 25-35 km, thinning to 16-18 km beneath  
146 the troughs, 20-21 km beneath the island of Pantelleria, and 24-25 km beneath the island of  
147 Linosa (Civile et al., 2008; Catalano et al., 2009). The depth to the lithosphere-asthenosphere  
148 boundary has been inferred from regional geophysical studies. The Pelagian Block is  
149 characterized by high heat flow (>80 mW/m<sup>2</sup>) with values that increase to >130 mW/m<sup>2</sup> in the

1  
2  
3  
4 150 Pantelleria and Linosa troughs (Della Vedova et al., 1995) and up to 200-460 mW/m<sup>2</sup> within the  
5  
6  
7 151 Cinque Denti caldera (Bellani et al., 1995). Combined with positive Bouguer anomalies (65-103  
8  
9 152 mgal; Berrino and Capuano, 1995), several workers have suggested asthenospheric upwelling up  
10  
11  
12 153 to ~60 km (Della Vedova et al., 1995; Argnani and Torelli, 2001; Civile et al., 2008).

13  
14 154 Extension of the SSRZ began ~7 Ma, with minor volcanism occurring during the late  
15  
16 155 Miocene (Messinian) and the vast majority of volcanism occurring during the Plio-Pleistocene  
17  
18  
19 156 (Calanchi et al., 1989; Rotolo et al., 2006; Coltelli et al., 2016; Lodolo et al., 2019; Martinelli et  
20  
21 157 al., 2019). Volcanic seamounts are primarily located in one of three areas within the SSRZ  
22  
23  
24 158 (Figure 1; Aissi et al., 2015): (1) the Graham and Terrible volcanic province (Anfirite, Tetide,  
25  
26 159 Galatea, Graham Bank, Cimotoc, Pinne, and Nameless Bank volcanoes), which lies 50-75 km  
27  
28  
29 160 offshore and runs parallel to the coast of Sicily for ~100 km between Mazara del Vallo and  
30  
31 161 Agrigento (Lodolo et al., 2019); (2) near the island of Pantelleria (Pantelleria SE, Pantelleria E,  
32  
33 162 Pantelleria SW, Pantelleria Central Bank, Angelia, and Foerstner volcanoes); and (3) north of the  
34  
35  
36 163 island of Linosa (Linosa I, Linosa II, and Linosa III volcanoes). Within the Graham and Terrible  
37  
38 164 volcanic province, the oldest (late Miocene) is the Nameless Bank seamount, which lies ~100 km  
39  
40  
41 165 east of Pantelleria and ~70 km southwest of Agrigento and rises from a depth of 330-340 m to  
42  
43 166 80-90 m b.s.l.; the youngest is the Graham Bank seamount, which is located ~50 km southwest  
44  
45  
46 167 of Sciacca and ~70 km northwest of Pantelleria, rises from 330-340 m to 7 m b.s.l., and last  
47  
48 168 erupted in 1831 CE (producing the ephemeral “Ferdinanda Island”; Gemmellaro, 1831;  
49  
50  
51 169 Washington, 1909; Kelly et al., 2014; Cavallaro and Coltelli, 2019.)

52  
53 170 The island of Pantelleria is by far the larger (83 km<sup>2</sup> surface area; 580 km<sup>2</sup> total) of the  
54  
55  
56 171 two islands and represents the emergent portion of a volcanic edifice that rises 836 m above sea  
57  
58 172 level and ~2200 m above the sea floor within the Pantelleria graben (Calanchi et al., 1989; Civile

1  
2  
3  
4 173 et al., 2010). Most rocks exposed on the island are felsic, volcanic (trachyte-pantellerite), and  
5  
6  
7 174 younger than the  $45.7 \pm 1.0$  ka pantelleritic Green Tuff, the caldera-forming ignimbrite of the  
8  
9 175 Cinque Denti caldera (Mahood and Hildreth, 1986; Scaillet et al., 2013). The oldest exposed  
10  
11  
12 176 pantelleritic lava on the island has been dated at  $324 \pm 11$  ka (Mahood and Hildreth, 1986), but  
13  
14 177 most of the island is submerged, much older, and most likely primarily basaltic (Fulignati et al.,  
15  
16 178 1997). The oldest documented basalts ( $\sim 80$ -120 ka, herein termed “paleo-Pantelleria”, following  
17  
18  
19 179 Avanzinelli et al., 2004) are exposed primarily in outcrops along the coast and along the scarp of  
20  
21 180 the Cinque Denti caldera (Mahood and Hildreth, 1986). Younger mafic lavas (“neo-Pantelleria”)  
22  
23  
24 181 are found in the northwestern part of the island and include flows that erupted at  $\sim 29$  ka from the  
25  
26 182 Cuddia Bruciata, Cuddia Ferle, and Cuddia del Monte cinder cones, and at  $\sim 10$  ka from the  
27  
28  
29 183 Cuddie Rosse cinder cone (Mahood and Hildreth, 1986; Civetta et al., 1998). The most recent  
30  
31 184 volcanic activity occurred  $\sim 4$  km NW of the island at the submarine (250 m b.s.l.) Foerstner  
32  
33  
34 185 volcano on 17-25 October 1891 CE (Washington, 1909; Conte et al., 2014; Kelly et al., 2014).

35  
36 186 The island of Linosa lies  $\sim 120$  km to the southeast of Pantelleria. Linosa is much smaller  
37  
38 187 ( $5.4 \text{ km}^2$  surface area;  $159 \text{ km}^2$  total) and represents the emergent portion of a large submarine  
39  
40  
41 188 volcanic complex that rises 196 m above sea level and  $\sim 800$  m above the sea floor along the SW  
42  
43 189 edge of the Linosa graben (Rossi et al., 1996; Tonielli et al., 2019; Romagnoli et al., 2020).  
44  
45  
46 190 Linosa is dominated by mafic lavas and tuffs that erupted in three stages at 1070 ka (paleo-  
47  
48 191 Linosa), 700 ka (Arena Bianca), and 530 ka (Monte Bandiera) and created several coalescing  
49  
50  
51 192 cinder cone and maar volcanoes (Lanzafame et al., 1994). The paleo-Linosa stage is  
52  
53 193 characterized primarily by hydromagmatic pyroclastic sequences with minor scoria and lava  
54  
55  
56 194 which built maars and cinder cones. The beginning of the Arena Bianca stage was dominated by  
57  
58 195 hydromagmatism followed by eruptions of scoria that built the Monte Nero cinder cone and lava  
59  
60  
61  
62  
63  
64  
65



1  
2  
3  
4  
5  
6  
7  
8  
9  
10  
11  
12  
13  
14  
15  
16  
17  
18  
19  
20  
21  
22  
23  
24  
25  
26  
27  
28  
29  
30  
31  
32  
33  
34  
35  
36  
37  
38  
39  
40  
41  
42  
43  
44  
45  
46  
47  
48  
49  
50  
51  
52  
53  
54  
55  
56  
57  
58  
59  
60  
61  
62  
63  
64  
65

196 flows that created the eastern third of the present-day island. The Monte Bandiera stage also  
197 began with hydromagmatic activity that created the Fossa Cappellano maar volcano (and  
198 associated Monte Bandiera tuff ring), which was followed by eruptions of scoria and lava that  
199 built the Montagna Rossa and Monte Vulcano cinder cones that dominate the western two-thirds  
200 of the island (Rossi et al., 1996).

201

### 3. Methods and Results

#### 3.1 Methods and materials

204 Twenty-two samples of mafic lava and scoria were collected from the islands of  
205 Pantelleria (12) and Linosa (10) during field trips in 2003, 2006 and 2013, six of which were  
206 originally presented in Parker and White (2008) and White et al. (2009). These samples were  
207 powdered to -200 mesh in a pre-contaminated shatterbox grinder and were analyzed at  
208 Activation Laboratories, Ontario, for major-elements by ICP-OES and trace-elements (including  
209 a full suite of rare earth elements [REE]) by ICP-MS (Code 4Lithoresearch). Whole-rock  
210 analyses are presented in Table 1. For the discussion that follows, these analyses are combined  
211 with data from literature for a total of 134 analyses of mafic rocks ( $\text{SiO}_2 \leq 52$  wt% normalized  
212 anhydrous); 75 of these include analyses of REE, including 39 from Pantelleria (Civetta et al.,  
213 1998; Esperança & Crisci, 1995; Avanzinelli et al., 2004, 2014), 29 from Linosa (Bindi et al.,  
214 2002; Di Bella et al., 2008; Avanzinelli et al., 2014), and 7 from various Seamounts (Rotolo et  
215 al., 2006; with additional data from Beccaluva et al., 1981, and Calanchi et al., 1989). Excluded  
216 are the Khartibucale hawaiiites at Pantelleria, which deserve a separate study; they have trace-  
217 element and isotopic signatures significantly different from the rest of the SSRZ mafic lavas and  
218 there are only three known published analyses, each of which is too evolved ( $\text{MgO} < 5$  wt%, Ni

1  
2  
3  
4 219 < 10 ppm) to be reliably used with the models presented in this study (Avanzinelli et al., 2004,  
5  
6  
7 220 2014; White et al., 2009).

### 8 9 221 *3.2 Major-element geochemistry*

10  
11 222 All but five samples classify as either basalt or hawaiiite (Figure 2a; Le Maitre, 2002),  
12  
13  
14 223 with basalts further classified based on normative mineralogy (assuming  $\text{FeO}/\text{FeO}^* = 0.9$ ) as  
15  
16 224 either alkali basalt (ol+ne-normative) or transitional basalt (ol+hy-normative) on their position in  
17  
18  
19 225 the basalt tetrahedron (Figure 2b; Irvine and Baragar, 1971). Linosa samples from the 1070 ka  
20  
21 226 paleo-Linosa and 530 ka Monte Bandiera stages are dominated by alkali basalt, with the samples  
22  
23  
24 227 evolving from Ol' (= normative ol + 0.25hy) towards normative Ab along the Ol'-Ab join, which  
25  
26 228 divides the “alkali” and “transitional” basalt fields. Linosa samples from the 700 ka Arena  
27  
28  
29 229 Bianca stage along with most Pantelleria samples classify predominantly as transitional basalts.  
30  
31 230 Mafic lavas and scoriae from both trends are petrographically broadly similar, consisting of  
32  
33 231 porphyritic rocks with variable amounts of phenocrysts of olivine, clinopyroxene, plagioclase,  
34  
35  
36 232 and magnetite (Rossi et al., 1996; Civetta et al., 1998; Bindi et al., 2002; Di Bella et al., 2008;  
37  
38 233 and White et al., 2009 provide comprehensive descriptions).

39  
40  
41 234 Major-element variation diagrams that use wt% MgO as a differentiation index are  
42  
43 235 plotted in Figure 3. Several differences can be seen between and within the Pantelleria and  
44  
45  
46 236 Linosa suites. Primitive basalts (MgO > 9 wt%) have not been documented at Pantelleria (max  
47  
48 237 7.65 wt%, median 5.82 wt% MgO), but have been at Linosa (max 16.35 wt%, median 7.72 wt%  
49  
50  
51 238 MgO). However, basalts with very high (>14 wt%) MgO at Linosa likely resulted from the  
52  
53 239 accumulation of olivine (Di Bella et al., 2008). At a given concentration of MgO, Linosa basalts  
54  
55  
56 240 have higher SiO<sub>2</sub> and Al<sub>2</sub>O<sub>3</sub>, but lower FeO\*, TiO<sub>2</sub>, and CaO than Pantelleria basalts (Figures 3a,  
57  
58 241 b, c, d, e). Within the Linosa samples, CaO increases with decreasing to MgO to ~8 wt% after  
59  
60  
61  
62  
63  
64  
65

1  
2  
3  
4  
5  
6  
7  
8  
9  
10  
11  
12  
13  
14  
15  
16  
17  
18  
19  
20  
21  
22  
23  
24  
25  
26  
27  
28  
29  
30  
31  
32  
33  
34  
35  
36  
37  
38  
39  
40  
41  
42  
43  
44  
45  
46  
47  
48  
49  
50  
51  
52  
53  
54  
55  
56  
57  
58  
59  
60  
61  
62  
63  
64  
65

242 which it decreases. Two distinct trends are observed in plots of TiO<sub>2</sub> and K<sub>2</sub>O versus MgO  
243 (Figures 3b, g). The higher-TiO<sub>2</sub>, K<sub>2</sub>O, and P<sub>2</sub>O<sub>5</sub> trend (labelled “A”, following Di Bella et al.,  
244 2008) includes most of the younger Monte Bandiera (MB) basalts from Linosa and some  
245 samples from the older suites; The lower- TiO<sub>2</sub>, K<sub>2</sub>O, and P<sub>2</sub>O<sub>5</sub> trend (labelled “B”, following Di  
246 Bella et al., 2008) includes most of the older Arena Bianca (AB) basalts from Linosa and some  
247 samples from both MB and the older Paleo-Linosa (PL) suites. The younger basalts from  
248 Pantelleria (neo-Pantelleria; NP) form trends similar to Trend B with respect to K<sub>2</sub>O (but at  
249 slightly lower values) and P<sub>2</sub>O<sub>5</sub> but with considerably higher TiO<sub>2</sub>, whereas the older basalts  
250 (paleo-Pantelleria; PP) define no coherent trend, and are characterized by even higher TiO<sub>2</sub> (>3  
251 wt%) and P<sub>2</sub>O<sub>5</sub> (>1 wt%) than the NP basalts (Civetta et al., 1998). Bindi et al. (2002) and Di  
252 Bella et al. (2008) attributed the origin of the two suites at Linosa as the result of fractional  
253 crystallization from similar, hypothetical parental basalts at different pressures, with “Trend-A”  
254 representing a younger suite that crystallized at higher pressures based on clinopyroxene crystal  
255 chemistry. In contrast, Civetta et al. (1998) attributed the differences between the High Ti-P and  
256 Low Ti-P suites of Pantelleria to variable degrees of partial melting from a heterogeneous mantle  
257 source in addition to fractional crystallization.

### 258 *3.3 Trace-element geochemistry*

259 Trace-element variation diagrams that use MgO as a differentiation index are plotted in  
260 Figure 4. As with the major-element geochemistry, trace-element concentrations and ratios show  
261 great diversity both between and within the island suites. Ni, Cr and Co (not shown),  
262 demonstrate a constant and linear decrease with MgO indicating fractionation (or accumulation  
263 in the case of high-MgO samples) of olivine throughout the suite. Unlike the transition elements,  
264 the large-ion lithophile elements (LILE: Rb, Sr, Ba, and La) and high field-strength elements

1  
2  
3  
4 265 (HFSE: Zr, Nb) form distinct trends, similar to K<sub>2</sub>O and TiO<sub>2</sub>. Trend-A is again dominated by  
5  
6  
7 266 the Monte Bandiera (MB) lavas from Linosa, and includes a few samples from the other Linosan  
8  
9 267 suites as well as some of the paleo-Pantelleria (PP) samples, whereas Trend-B consists of the  
10  
11 268 Arena Bianca (AB) lavas from Linosa as well as a few samples from the other Linosan suites as  
12  
13  
14 269 well as most of the neo-Pantelleria (NP) samples and some of the PP samples. At a given value  
15  
16 270 of MgO, the NP samples demonstrate slightly lower values of Rb, Zr, Nb, and La than the MB  
17  
18  
19 271 samples.

20  
21 272         Representative rare earth element (REE) diagrams (normalized to CI chondrite;  
22  
23  
24 273 McDonough and Sun, 1995) are presented in Figure 5. Arena Bianca (AB; Figure 5b) and neo-  
25  
26 274 Panelleria (NP; Figure 5e) display the most constant values, with La<sub>N</sub>/Yb<sub>N</sub> enrichments of ~7.0  
27  
28  
29 275 and 9.5 and Sm<sub>N</sub>/Yb<sub>N</sub> enrichments of ~2.7 and 3.8, respectively. Monte Bandiera (MB; Figure  
30  
31 276 5c) has a large range of La<sub>N</sub>/Yb<sub>N</sub> values, but near-constant Sm<sub>N</sub>/Yb<sub>N</sub>. Paleo-Linosa samples (PL;  
32  
33  
34 277 Figure 5a) have similar HREE concentrations, but La<sub>N</sub>/Yb<sub>N</sub> values either more similar to AB or  
35  
36 278 MB. Paleo-Pantelleria (PP) and the seamounts (SEA) have the least internal consistency, at least  
37  
38 279 in part because unlike the others they represent discrete volcanic centers that erupted over ~120  
39  
40  
41 280 ka and 8 Ma, respectively. Several PP samples have La<sub>N</sub>/Yb<sub>N</sub> and Sm<sub>N</sub>/Yb<sub>N</sub> ratios similar to NP.  
42  
43 281 Positive Eu anomalies (i.e., Eu<sub>N</sub>/Eu\* > 1.0, with Eu\* = [Sm<sub>N</sub> · Gd<sub>N</sub>]<sup>1/2</sup>) characterize basalts on  
44  
45  
46 282 both islands, with Pantelleria basalts (PP Eu<sub>N</sub>/Eu\* = 1.13 ± 0.17; NP Eu<sub>N</sub>/Eu\* = 1.17 ± 0.09)  
47  
48 283 having a more pronounced anomaly than Linosa basalts (Eu<sub>N</sub>/Eu\* = 1.06 ± 0.07). Positive Eu  
49  
50  
51 284 anomalies are a common feature in primitive (MgO > 9 wt%) MORB and OIB and have been  
52  
53 285 interpreted as evidence of mixing of DMM with recycled lower continental lithosphere (Niu and  
54  
55 286 O'Hara, 2009; Tang et al., 2015); however, the lack of a negative correlation between Eu<sub>N</sub>/Eu\*  
56  
57  
58 287 and radiogenic lead isotope ratios makes lower continental crust an unlikely component.

1  
2  
3  
4  
5  
6  
7  
8  
9  
10  
11  
12  
13  
14  
15  
16  
17  
18  
19  
20  
21  
22  
23  
24  
25  
26  
27  
28  
29  
30  
31  
32  
33  
34  
35  
36  
37  
38  
39  
40  
41  
42  
43  
44  
45  
46  
47  
48  
49  
50  
51  
52  
53  
54  
55  
56  
57  
58  
59  
60  
61  
62  
63  
64  
65

288 Likewise, the ubiquity of the positive Eu anomaly in SSRZ basalts coupled with its presence in  
289 aphyric and low-phyric basalts, along with a lack of correlation between  $Eu_N/Eu^*$  and Sr,  
290 strongly suggests that plagioclase accumulation is an unlikely mechanism for producing this  
291 anomaly in these rocks (Civetta et al., 1998; Bindi et al., 2002; Di Bella et al., 2008; White et al.,  
292 2009). Alternatively, a positive Eu anomaly may simply be due the relative incompatibility of  
293 divalent Eu in clinopyroxene compared to trivalent Gd and Sm, coupled with more reducing  
294 conditions in the source region which leads to higher  $Eu^{2+}/Eu^{3+}$  and thus higher  $Eu_N/Eu^*$  in the  
295 partial melts (Tang et al., 2017).

## 297 **4.0 Discussion**

### 298 *4.1. Fractional crystallization and magma storage*

299 Models of fractional crystallization/accumulation processes and magma storage  
300 conditions are evaluated using Pearce (1968) element ratio (PER) diagrams coupled with the  
301 results of thermodynamic (MELTS) modelling. PER diagrams plot ratios of major elements or  
302 combinations of major elements with a common incompatible, or “conserved”, element (e.g.,  
303 Mg/K vs. Ca/K or [Si+Al]/Zr vs. [Na+K]/Zr). Interpretations of these diagrams are based on the  
304 stoichiometry of rock-forming minerals, and slopes of data distributions are equal to major  
305 element ratios of minerals lost or gained during differentiation of a cogenetic suite of rocks  
306 (Russell and Nicholls, 1988). For example, data plotted with Mg/K on the abscissa and Ca/K or  
307 Al/K on the ordinate will form a linear trend with a slope that varies depending on the  
308 fractionating or accumulating assemblage from horizontal for a phase with non-stoichiometric  
309 Ca or Al (e.g., olivine) to vertical for a phase with non-stoichiometric Mg (e.g., plagioclase).  
310 Diagrams plotting Mg/K versus Al/K (Figure 6a) and Ca/K (Figure 6b) can therefore be used to

1  
2  
3  
4 311 discriminate between fractionation or accumulation of olivine (horizontal slopes on both  
5  
6 312 diagrams with decreasing Mg/K), clinopyroxene (horizontal slope with Al/K and a positive slope  
7  
8 313 with Ca/K versus Mg/K), and plagioclase (positive slopes on both diagrams). The two Linosa  
9  
10 314 trends (hereafter LIN-A and LIN-B) observed in the major- and trace-element variation diagrams  
11  
12 315 (Figures 3 and 4) are also seen in the PER diagrams. These first preclude the possibility of a  
13  
14 316 common parental magma for the two trends; linking LIN-A and LIN-B by fractional  
15  
16 317 crystallization would require the crystallization of geologically implausible mineral assemblages.  
17  
18 318 PER diagrams suggest that LIN-A is formed by a paragenetic sequence of olivine to olivine +  
19  
20 319 clinopyroxene to clinopyroxene + plagioclase ± olivine and LIN-B is formed by a continuous  
21  
22 320 sequence of plagioclase + clinopyroxene ± olivine. Samples with Mg/K > 12 correspond to  
23  
24 321 those with MgO > 14 wt% and are most likely the result of olivine accumulation. Both trends  
25  
26 322 converge at Mg/K ≈ 4, which corresponds to MgO ≈ 6.5 wt%. Pantelleria basalts form a trend  
27  
28 323 subparallel to LIN-B, suggesting that these magmas evolved along a similar liquid line of  
29  
30 324 descent.

31  
32  
33 325         These interpretations are in accord with the results of thermodynamic models of  
34  
35 326 fractional crystallization. Models were produced using the MELTS algorithm (rhyolite-MELTS  
36  
37 327 v. 1.0.2; Ghiorso and Sack, 1995; Asimow and Ghiorso, 1998; Gualda et al., 2012), the results of  
38  
39 328 which are superimposed on the data in Figure 6. The models presented were calculated under  
40  
41 329 anhydrous conditions with oxygen fugacities fixed to the fayalite-magnetite-quartz (FMQ) buffer  
42  
43 330 and a step size of 5°C. LIN-A is most successfully modeled as fractional crystallization from the  
44  
45 331 most primitive MB basalt (LSN51, 12.59 wt% MgO, Mg# = 0.70, 278 ppm Ni; Di Bella et al.,  
46  
47 332 2008) at 0.65 GPa. At this pressure olivine is the liquidus phase at 1376°C, and is replaced by  
48  
49 333 clinopyroxene at 1281°C (MgO<sup>liq</sup> = 8.83 wt%, F = 0.89), which is joined by plagioclase at  
50  
51  
52  
53  
54  
55  
56  
57  
58  
59  
60  
61  
62  
63  
64  
65

1  
2  
3  
4 334 1191°C ( $\text{MgO}^{\text{liq}} = 4.40 \text{ wt\%}$ ,  $F = 0.56$ ). In contrast, LIN-B is best modelled as the result of  
5  
6 335 fractional crystallization from the most primitive AB basalt (LNS40, 7.68 wt% MgO,  $\text{Mg\#} =$   
7  
8 336 0.59, 85 ppm Ni; Bindi et al., 2002) at 0.2. At this pressure, olivine is the liquidus phase at  
9  
10 337 1206°C, and is closely joined by plagioclase at 1201°C ( $\text{MgO}^{\text{liq}} = 7.45 \text{ wt\%}$ ,  $F = 0.95$ ), and  
11  
12 338 clinopyroxene at 1196°C ( $\text{MgO}^{\text{liq}} = 7.26 \text{ wt\%}$ ,  $F = 0.89$ ). These models are consistent with the  
13  
14 339 mass balance models discussed by Di Bella et al. (2008) and the conclusions of Bindi et al.  
15  
16 340 (2002), who used evidence from clinopyroxene crystal chemistry to suggest that the depth and  
17  
18 341 pressure of fractional crystallization at Linosa increased with time from 700 ka (AB) to 530 ka  
19  
20 342 (MB). Assuming average crustal density of 2700 kg/m<sup>3</sup>, this places the magma reservoir at ~7.6 km  
21  
22 343 for the largely older LIN-B suite and ~24.6 km for the younger LIN-A suite; these values  
23  
24 344 correspond closely to the depths of the top of the crystalline basement (~8 km) and the Moho  
25  
26 345 (24-25 km) beneath Linosa, respectively (Civile et al., 2008). Thermodynamic models for the  
27  
28 346 younger Pantelleria basalts (NP) reported by White et al. (2009) have results similar to LIN-B,  
29  
30 347 but require lower pressures (0.10 GPa) and more hydrous conditions (1.0-1.5 wt% H<sub>2</sub>O) with  
31  
32 348 olivine on the liquidus at  $1135 \pm 10^\circ\text{C}$ , followed by clinopyroxene at  $1125 \pm 10^\circ\text{C}$  and plagioclase  
33  
34 349 at  $1085 \pm 10^\circ\text{C}$ .

#### 350 *4.2 Primary magma compositions and constraints on pressure and temperature of melt* 351 *generation*

352 An estimate of the composition of primary basalts is necessary to determine the  
353 conditions of partial melting in the mantle, such as the temperature, pressure/depth of melt  
354 segregation, and melt fraction produced. However, every basalt has undergone some degree of  
355 fractionation and assimilation prior to eruption and even if assimilation is assumed to be  
356 negligible, once the fractionating magma is multiply saturated it becomes very difficult to back-

1  
2  
3  
4  
5  
6  
7  
8  
9  
10  
11  
12  
13  
14  
15  
16  
17  
18  
19  
20  
21  
22  
23  
24  
25  
26  
27  
28  
29  
30  
31  
32  
33  
34  
35  
36  
37  
38  
39  
40  
41  
42  
43  
44  
45  
46  
47  
48  
49  
50  
51  
52  
53  
54  
55  
56  
57  
58  
59  
60  
61  
62  
63  
64  
65

357 calculate the liquid line of decent (O'Hara, 1968). To do so, of course, first requires the  
358 assumption that the rock sample is relatively unweathered and has undergone only olivine  
359 fractionation; for this reason, we include only relatively primitive samples characterized by very  
360 low (<1 wt%) LOI, relatively high (>10 wt%) MgO, and a lack of a negative Eu anomaly. We  
361 also exclude those with very high (>14 wt%) MgO, which could be the result of olivine  
362 accumulation (Di Bella et al., 2008). The only samples that fit these criteria are those fall along  
363 the olivine fractionation trend for LIN-A in Figure 6 (discussed in section 4.1). Therefore most of  
364 the remainder of the discussion will focus on the origin of the basalts of this sub-group, with  
365 inferences made for the origin of the others by comparison.

366         The composition of the primary magma parental to a basaltic rock may be estimated by  
367 iteratively “correcting” it for olivine fractionation until the recalculated basalt has an Mg# that  
368 has been experimentally determined to be in equilibrium with mantle peridotite (Lee et al.,  
369 2009). Calculated (anhydrous) primary basalts in equilibrium with peridotite with an olivine  
370 composition of  $F_{O_{90}}$  and  $Fe^{3+}/\Sigma Fe = 0.13$  (estimated following Cottrell and Kelley, 2013) for all  
371 samples that meet the criteria above ( $n = 17$ ) are very similar, classifying as alkali basalts with  
372  $SiO_2 = 46.08 \pm 0.16$  wt%,  $TiO_2 = 1.94 \pm 0.06$  wt%,  $Al_2O_3 = 13.05 \pm 0.51$  wt%,  $Fe_2O_3 = 1.41 \pm$   
373  $0.02$  wt%,  $FeO = 9.55 \pm 0.16$  wt%,  $MnO = 0.16 \pm 0.01$ ,  $MgO = 15.18 \pm 0.27$  wt%,  $CaO = 8.57 \pm$   
374  $0.42$  wt%,  $Na_2O = 2.60 \pm 0.24$  wt%, and  $K_2O = 1.19 \pm 0.08$  wt% (Table 2). Primary basalts  
375 calculated from starting basalt compositions with 1 wt%  $H_2O$  have compositions that differ by  
376 <1% from each of these values, with the obvious exception of  $H_2O$  ( $0.90 \pm 0.01$  wt%). The  
377 olivine-liquid thermobarometer of Lee et al. (2009) provides a weighted average of the  
378 temperature and pressure of polybaric melting for the calculated primary basalts of  $1449 \pm 8^\circ C$   
379 and  $2.57 \pm 0.09$  GPa for anhydrous basalts and  $1422 \pm 7^\circ C$  and  $2.50 \pm 0.07$  GPa for hydrous



1  
2  
3  
4 380 basalts; individual values reported in Table 2 are plotted in Figure 7 along with the anhydrous  
5  
6  
7 381 and hydrous (116 ppm H<sub>2</sub>O, following Salters and Stracke, 2004) peridotite solidus (Katz et al.,  
8  
9 382 2003), the estimated limits of spinel and garnet stability (following Klemme and O'Neill, 2000),  
10  
11 383 and the approximate lithosphere-asthenosphere boundary (60 km; Civile et al., 2008). The  
12  
13 384 calculated average pressures of segregation correspond to depths of  $83.2 \pm 2.6$  km (anhydrous)  
14  
15  
16 385 and  $81.1 \pm 2.2$  km (hydrous) which places their origin within the garnet-spinel transition zone,  
17  
18 386 consistent with the interpretation of previous workers (Mahood and Baker, 1986; Civetta et al.,  
19  
20 387 1998; Di Bella et al., 2008; Avanzinelli et al., 2014). These results suggest a mantle potential  
21  
22 388 temperature between  $1415 \pm 7$  and  $1435 \pm 8^\circ\text{C}$ , with calculated melt fractions of  $0.019 \pm 0.011$   
23  
24 389 (anhydrous) to  $0.027 \pm 0.009$  (hydrous) under those conditions (Langmuir et al., 1992; Putirka,  
25  
26 390 2005; Putirka et al., 2007; Supplementary Data 1). Also plotted in Figure 7 are the isentropic  
27  
28 391 partial melting paths for both (a) anhydrous and (b) hydrous (116 ppm H<sub>2</sub>O) average DMM  
29  
30 392 (Salters and Stracke, 2004). These paths were calculated with the pMELTS algorithm (v.5.6.1;  
31  
32 393 Ghiorso et al., 2002) from the intersections of the (a) dry lherzolite solidus (Katz et al., 2003)  
33  
34 394 with the  $1435^\circ\text{C}$  adiabat (3.32 GPa or  $\sim 106$  km,  $1470^\circ\text{C}$ ) and the (b) hydrous lherzolite solidus  
35  
36 395 with the  $1415^\circ\text{C}$  adiabat (3.62 GPa or  $\sim 116$  km,  $1452^\circ\text{C}$ ) to the base of the lithosphere (1.8 GPa,  
37  
38 396 corresponding to  $\sim 60$  km). Both melting models were calculated with oxygen fugacities fixed at  
39  
40 397 the FMQ buffer and a step size of 50 bars ( $\sim 155$  m) and both predict final melt fractions of 2.2-  
41  
42 398 2.5%, consistent with the value estimated from olivine-liquid thermobarometry. Model  
43  
44 399 temperatures are higher than those determined for "ambient" MORB mantle ( $T_p \approx 1350^\circ\text{C}$ , 0.7-  
45  
46 400 1.7 GPa; Lee et al., 2009) and similar to those determined for extension-related intraplate  
47  
48 401 volcanism. Examples can be found in the Basin and Range province where the continental  
49  
50 402 lithosphere has been similarly thinned, such as Owens Valley (southeastern California, USA;  
51  
52  
53  
54  
55  
56  
57  
58  
59  
60  
61  
62  
63  
64  
65

1  
2  
3  
4 403 ~1425°C, 60-80 km; Lee et al., 2009) and Snow Canyon (southwestern Utah, USA; ~1422°C, 58  
5  
6 404 km; Plank and Forsythe, 216).

7  
8  
9 405 Various tests have been proposed to determine the source material for basalts based on  
10  
11 406 their major-element content, but these provide equivocal results for Pantelleria and Linosa. The  
12  
13 407 calculated composition of primary magma for Linosa-A places it within the field of experimental  
14  
15 408 partial melts of peridotite (Dasgupta et al., 2010), although the PRIMELTS3 algorithm places it  
16  
17 409 in the field of partial melts of “pyroxenite” (Herzberg and Asimow, 2008). The Yang and Zhou  
18  
19 410 (2013) test for mantle source composition is also equivocal: the FC3MS (wt%  $\text{FeO}^T/\text{CaO} -$   
20  
21 411  $3\text{MgO}/\text{SiO}_2$ ) value of the calculated primary basalts ( $0.26 \pm 0.07$ ) is within the range for both  
22  
23 412 peridotite ( $-0.07 \pm 0.51$ ) and pyroxenite ( $0.46 \pm 0.96$ ) partial melts. Other major-element ratios  
24  
25 413 purported to flag source compositions for basalts include  $\text{CaO}/\text{Al}_2\text{O}_3$ ,  $\text{K}_2\text{O}/\text{TiO}_2$  (Jackson and  
26  
27 414 Dasgupta, 2008), and  $\text{Fe}/\text{Mn}$  (Davis et al., 2013) and provide similarly ambiguous results:  
28  
29 415  $\text{CaO}/\text{Al}_2\text{O}_3$  ( $0.65 \pm 0.05$ ) and  $\text{K}_2\text{O}/\text{TiO}_2$  ( $0.61 \pm 0.04$ ) plot nearest the EM1 component and  
30  
31 416 furthest from the MORB-HIMU array, inconsistent with isotopic evidence; and  $\text{Fe}/\text{Mn}$  for all  
32  
33 417 basalts from both islands is  $61.1 \pm 5.6$ , which is at the proposed boundary (62) for peridotite- vs.  
34  
35 418 eclogitic-derived melts. Therefore, we suggest that although these tests provide inconclusive  
36  
37 419 results, they also suggest that that unenriched DMM alone is an unlikely source for LIN-A  
38  
39 420 magmas specifically or for SSRZ basalts in general.  
40  
41  
42  
43  
44  
45  
46  
47

48 421 Relatively high concentrations of  $\text{TiO}_2$  in the basalts may also support this hypothesis, as  
49  
50 422 well as point to a greater role for eclogite in the source of Pantelleria basalts compared to Linosa.  
51  
52 423 Following Prytulak and Elliot (2007), calculated values of  $\text{Ti}_8$  (viz., the regressed value of  $\text{TiO}_2$   
53  
54 424 at 8 wt% MgO) for SSRZ basalts are 1.9 (LIN-B), 2.3 (LIN-A), and 3.0 (PNL-L); these  
55  
56  
57 425 correspond to minimum concentrations (for  $F = 0.01$  to  $0.10$ ) of  $\text{TiO}_2$  in the mantle source of  
58  
59  
60  
61  
62  
63  
64  
65

1  
2  
3  
4  
5  
6  
7  
8  
9  
10  
11  
12  
13  
14  
15  
16  
17  
18  
19  
20  
21  
22  
23  
24  
25  
26  
27  
28  
29  
30  
31  
32  
33  
34  
35  
36  
37  
38  
39  
40  
41  
42  
43  
44  
45  
46  
47  
48  
49  
50  
51  
52  
53  
54  
55  
56  
57  
58  
59  
60  
61  
62  
63  
64  
65

426 ~0.2-0.3 wt% for Linosa and ~0.3-0.5 wt% for Pantelleria compared to a range of ~0.13 wt%  
427 (DMM; Salters and Stracke, 2004) to ~0.20 wt% (PM; McDonough and Sun, 1995). Given an  
428 average concentration of 1.3 wt% TiO<sub>2</sub> in MORB (Sun and McDonough, 1989), these  
429 concentrations could be achieved by 5-15% recycled MORB (as eclogite) mixed with DMM for  
430 Linosa and 15-30% for Pantelleria. Additionally, the high concentrations of P<sub>2</sub>O<sub>5</sub> that  
431 accompany elevated TiO<sub>2</sub> in the Pantelleria basalts may also indicate a higher presence of  
432 eclogite in their mantle source (Haggerty et al., 1994).

433 *4.3 Trace element constraints on partial melting and mantle sources*

434 The isotopic heterogeneity of the mantle is an acquired feature, but how it correlates with  
435 lithological heterogeneity is much less certain (Zindler and Hart, 1986; Dasgupta et al., 2010;  
436 Stracke, 2012). As noted in the Introduction, there is very little variability with respect to Sr and  
437 Nd isotopes in the SSRZ basalts (with the exception of the seamounts, which have high LOI [3.7  
438 ± 2.5 wt%] and therefore may have been strongly affected by seawater weathering; Rotolo et al.,  
439 2006). Despite this apparent isotopic homogeneity with respect to Sr-Nd-He, the data clearly  
440 show several significant differences with respect to major- and trace-element compositions (and  
441 Pb isotopes; Avanzinelli et al., 2014) as well as some key similarities.

442 K/Nb and Nb/U ratios for Pantelleria (214 ± 38 and 49 ± 18) and Linosa (229 ± 22 and  
443 46 ± 6) basalts are similar to global values for OIB (253 ± 71 and 47 ± 10; Hofmann et al., 1986;  
444 Halliday et al., 1995; Arevalo et al., 2009) and, combined with Sr-Nd-Pb-O isotope systematics  
445 and U-series disequilibrium, argue strongly against a significant role for crustal contamination or  
446 assimilation in the origin of these basalts (Avanzinelli et al., 2014). Pantelleria and Linosa also  
447 have similar incompatible trace element ratios for Th/U (3.3 ± 0.8 and 3.2 ± 1.6), U/Pb (0.59 ±  
448 0.08 and 0.57 ± 0.16), Lu/Hf (0.08 ± 0.01 and 0.07 ± 0.01), and Rb/Sr (0.04 ± 0.01 and 0.05 ±

1  
2  
3  
4 449 0.01) which are characteristic of HIMU end-member OIBs (Willbold and Stracke, 2006).  
5  
6  
7 450 Despite these similarities, there are several systematic differences in other trace element ratios  
8  
9 451 both between and within the islands and seamounts.

10  
11 Ratios of incompatible trace elements (with REE ratios normalized to CI chondrite;  
12  
13  
14 453 McDonough and Sun, 1995) are presented in Figure 8.  $La_N/Yb_N$  is plotted against ppm La in  
15  
16 454 Figure 8a and shows a clear positive slope, strongly suggesting that variable degrees of partial  
17  
18  
19 455 melting are at least partially responsible for compositional variation in these magmas, with the  
20  
21 456 higher values representing smaller melt fractions (e.g., Mahood and Baker, 1986). A plot of  
22  
23  
24 457  $Sm_N/Yb_N$  versus  $La_N/Yb_N$  (Figure 8b) reveals four sub-groups, which we term LIN-A  
25  
26 458 (corresponding to the Linosa Trend-A described above), LIN-B (Linosa Trend-B), PNL-L  
27  
28  
29 459 (consisting of neo-Pantelleria and geochemically similar paleo-Pantelleria samples), and PNL-H  
30  
31 460 (which includes both the high-Ti and P paleo-Pantelleria and the Seamount samples). The lack  
32  
33  
34 461 of collinearity between these sub-groups suggests that, although internal variation within them  
35  
36 462 may be attributed to varying degrees of partial melting or fractional crystallization, the  
37  
38  
39 463 differences in  $Sm_N/Yb_N$  at a given value of  $La_N/Yb_N$  requires different mantle sources, with the  
40  
41 464 higher  $Sm_N/Yb_N$  sub-groups sources being higher in garnet.  $La_N/Sm_N$  is a sensitive indicator of  
42  
43 465 partial melting, and therefore its overall positive correlation with  $La_N/Yb_N$  (Figure 8c) reinforces  
44  
45  
46 466 variation both between and within the groups as attributable to variable melt fractions; however,  
47  
48 467 as with  $Sm_N/Yb_N$ , the different trends formed by the Linosa and Pantelleria groups strongly point  
49  
50  
51 468 to compositionally different mantle source regions. This is also seen in a plot of  $Dy/Dy^*$  versus  
52  
53 469  $Dy_N/Yb_N$  (Figure 8d), which reveals three subparallel trends. In this diagram, sub-suite trends  
54  
55  
56 470 with higher  $Dy_N/Yb_N$  also indicate a source more enriched in garnet, and the diagonal variability  
57  
58 471 within each trend can be attributed to differentiation (Davidson et al., 2013). The presence of  
59  
60  
61  
62  
63  
64  
65

1  
2  
3  
4 472 eclogite in the PNL-L source region (and for most of the paleo-Pantelleria samples in PNL-H)  
5  
6  
7 473 may be flagged by the decoupled behavior of  $Sm_N/Yb_N$  and  $Zr/Yb$  seen in Figure 8e.  
8  
9 474 Experimental work has shown that  $Zr$  is much less incompatible and possibly compatible in  
10  
11 475 grossular-rich (eclogitic) garnet compared to pyrope-rich (peridotitic) garnet, whereas  $D_{Sm}/D_{Yb}$  is  
12  
13  
14 476 similar in both lithologies (van Westrenen et al., 2001; Pertermann et al., 2004; Stracke and  
15  
16 477 Bourdon, 2009). Avanzinelli et al. (2014) documented a negative correlation between  $^{206}Pb/^{204}Pb$   
17  
18  
19 478 and  $Rb/La$  within the SSRZ basalts and suggested that this ratio may be used as a tracer of  
20  
21 479 recycled MORB in the source region following Willbold and Stracke (2006), who demonstrated  
22  
23  
24 480 that  $(Rb,Ba,K)/La$  ratios are systematically lower in basalts sourced from HIMU-like mantle.  
25  
26 481 The negative correlation between  $Sm_N/Yb_N$  and  $Rb/La$  in these suites (Figure 8f) coupled with  
27  
28  
29 482 the observations above may therefore provide further evidence for eclogite in the mantle source.  
30  
31 483 From these observations, we hypothesize: (1) LIN-A and LIN-B are not related by fractional  
32  
33 484 crystallization processes; (2) LIN-A and LIN-B have similar  $Dy_N/Yb_N$  and therefore may have  
34  
35  
36 485 similar mantle sources with respect to garnet, with LIN-B derived from a higher melt fraction;  
37  
38  
39 486 (3) the PNL sub-groups cannot be related via fractional crystallization; and (4) PNL-L and PNL-  
40  
41 487 H are either derived from different mantle sources or their differences reflect different degrees of  
42  
43 488 partial melting, with the relatively lower-melt fraction PNL-H sub-suite preserving more of the  
44  
45  
46 489 signal of the more fusible, recycled material (possibly as eclogite). Due to the scarcity of data  
47  
48 490 (isotope and REE data are only available for Graham Bank, Nameless Bank, and Pantelleria SE)  
49  
50  
51 491 and the lack of unaltered samples, it is more difficult to draw conclusions for the origin of the  
52  
53 492 seamounts, but their very high  $La/Yb$  ratios point to melt fractions lower than Linosa (i.e., ~1%)  
54  
55  
56 493 and the generally higher values of  $Sm/Yb$ ,  $TiO_2$ , and  $P_2O_5$  for Graham Bank and Nameless Bank  
57  
58  
59  
60  
61  
62  
63  
64  
65

1  
2  
3  
4 494 may be attributed to magma generation away from the rift grabbens and beneath thicker  
5  
6  
7 495 lithosphere (cf. Niu et al., 2011).

8  
9 496 Spider diagrams of representative analyses from each of the sub-groups ordered by  
10  
11 497 increasing compatibility in oceanic basalts (following Sun and McDonough, 1989) and  
12  
13  
14 498 normalized to DMM (Salters and Stracke, 2004) are presented in Figure 9. These are plotted  
15  
16 499 with the results of 2% ( $F = 0.02$ ) non-modal fractional melting of depleted garnet peridotite (GD)  
17  
18  
19 500 and spinel peridotite (SD) (see Supplementary Data 2 for details.) The model results for partial  
20  
21 501 melting of DMM form patterns very similar to those formed by all four sub-groups. Most  
22  
23  
24 502 notably, all groups form trends that run subparallel to the model results with excellent fits for the  
25  
26 503 LREE and more compatible elements, consistent with a similar origin by small degrees of partial  
27  
28  
29 504 melting of depleted peridotite in the spinel-garnet transition zone followed by fractional  
30  
31 505 crystallization. However, several notable anomalies require additional explanation: (1) in  
32  
33  
34 506 addition to DMM, the source regions for all four groups require a source component enriched in  
35  
36 507 LILE; (2) a positive P anomaly is present in both PNL groups, and is especially prominent in the  
37  
38  
39 508 PNL-H lavas; (3) PNL suites are characterized by relatively high Ti and low Zr; and (4) the  
40  
41 509 strong variability in PNL-H LILE contents and ratios strongly suggests that several different  
42  
43 510 components must be present in the source region for these diverse magmas which clearly must  
44  
45  
46 511 not be related by either partial melting or fractional crystallization processes.

47  
48 512 Therefore, we posit: (1) all magmas originate in the spinel-garnet transition zone from a  
49  
50  
51 513 source region dominated by DMM peridotite (Civetta et al., 1998; Neave et al., 2012;  
52  
53 514 Avanzinelli et al., 2014); (2) first-order differences between Pantelleria and Linosa/Seamounts  
54  
55  
56 515 are due to a greater amount of lithologically-enriched and possibly eclogitic material mixed with  
57  
58 516 peridotite in the former (cf. Avanzinelli et al., 2014); (3) differences between the Seamounts,

1  
2  
3  
4 517 LIN-A, and LIN-B are due to variable degrees of partial melting, with the Seamounts and  
5  
6  
7 518 Linosa-B being derived from the lowest and highest degrees of partial melting respectively; (4)  
8  
9 519 compositional diversity within the paleo-Pantelleria suite must reflect the presence of additional  
10  
11 520 diverse components in the mantle source and indicate mantle heterogeneity at the inter-island  
12  
13  
14 521 (10s of km) scale beneath Pantelleria (cf. Civetta et al., 1998); and (5) compositional  
15  
16 522 homogeneity in the LIN-B and PNL-L is probably due to homogenization in high-level magma  
17  
18  
19 523 reservoirs (see Figure 6), which obfuscates the variability from partial melting seen in LIN-A  
20  
21 524 and heterogeneity observed in PNL-H (e.g., McGee and Smith, 2016). In most PNL-L samples  
22  
23  
24 525 and some PNL-H samples there is also a positive Ba anomaly which may be the result of a small  
25  
26 526 amount of assimilation of high-Ba alkali feldspar cumulate rock at Pantelleria (White et al.,  
27  
28  
29 527 2012; Wolff, 2017).

#### 30 31 528 *4.4 Trace element models of partial melting*

32  
33 529 Whole-rock REE concentrations, along with major- and selected trace-element  
34  
35  
36 530 concentrations, were used to model the conditions of partial melting beneath Pantelleria and  
37  
38  
39 531 Linosa by means of the INVMEL program (McKenzie and O’Nions, 1991, 1995, 1998) as  
40  
41 532 modified by White et al. (1992). This program inverts REE geochemical data to find the best-fit  
42  
43 533 relationship between melt fraction and depth utilizing the partitioning behavior of a full suite of  
44  
45  
46 534 REE in mantle phases (Neave et al., 2012). It does this by running an initial forward non-modal  
47  
48 535 fractional melting model with trial parameters, predicting the weighted average composition of  
49  
50  
51 536 the fractional melt, calculating the root-mean square (RMS) error between the predicted and  
52  
53 537 observed calculations, and then adjusting the melt depth and degree curve to iteratively minimize  
54  
55  
56 538 the error. After the best-fit parameters producing the least misfit have been determined, a final  
57  
58 539 forward non-modal fractional melting model is run through the remaining major- and trace-

1  
2  
3  
4 540 element data to evaluate the robustness of fit. Results are considered acceptable if  $RMS < 1$  and  
5  
6  
7 541 the melting curve is relatively smooth. The program also estimates the quantity of olivine and  
8  
9 542 clinopyroxene fractionation (F), and the final melt fraction is adjusted by multiplication by  $1/(1-$   
10  
11  
12 543 F). The mantle source is set with the  $\epsilon_{Nd}$  parameter, which calculates a mixture of DMM ( $\epsilon_{Nd} =$   
13  
14 544  $+10, 0.815$  ppm Nd) and bulk silicate earth (“Primitive” Mantle, PM:  $\epsilon_{Nd} = 0, 1.08$  ppm Nd)  
15  
16 545 (McKenzie and O’Nions, 1991, 1998). The latter component does not necessarily represent  
17  
18  
19 546 primitive mantle or deep mantle plume material, but serves as a proxy for various enriched  
20  
21  
22 547 components such as recycled oceanic lithosphere that are well-mixed with peridotite and whose  
23  
24 548 compositions are not well-constrained (Gibson and Geist, 2010). Model mineral proportions and  
25  
26 549 chemical composition of DMM and PM sources are from McKenzie and O’Nions (1991, 1995),  
27  
28  
29 550 with the mineral-liquid trace element partition coefficients compiled by Gibson and Geist (2010)  
30  
31 551 (See Supplementary Data 2).

32  
33  
34 552 Inversion models for the three subgroups that are plausibly cogenetic (LIN-A, LIN-B,  
35  
36 553 and PNL-L) are presented in Figure 10. Average  $\epsilon_{Nd}$  values from Linosa (5.89) were used to set  
37  
38  
39 554 the mantle source region for both LIN-A and LIN-B, which corresponds to a mix of 66% DMM  
40  
41 555 and 34% PM; the average  $\epsilon_{Nd}$  for Pantelleria used in the models (6.33) was used to set the mantle  
42  
43  
44 556 source region for PNL-L, which corresponds to a mix of 70% DMM and 30% PM. Models were  
45  
46 557 calculated with the garnet-spinel transition zone fixed at 73-93 km (based on a mantle potential  
47  
48  
49 558 temperature of 1435°C; Klemme and O’Neill, 2000), while the top and bottom of the melting  
50  
51 559 column were allowed to vary. All models fit the observed REE data well and within  $1\sigma$  (Figures  
52  
53  
54 560 10a, b, c) with the exception of Eu in the PNL-L model, which is slightly higher. In the forward  
55  
56 561 models (Figures 10d, e, f), the results also fit the observed major and trace element data well,  
57  
58  
59 562 with a few notable exceptions: observed Th and Nb values are ubiquitously higher (68-83% and  
60  
61  
62  
63  
64  
65



1  
2  
3  
4 563 53-73% respectively) than model results for both islands, but within error, and observed Sr and  
5  
6  
7 564 Zr values are lower (50% and 17-28% respectively) than model results for Linosa, but within  $1\sigma$   
8  
9 565 and below that at Pantelleria. The models with the best fits have the tops of the melting columns  
10  
11 566 at 59-60 km and bases of the melting columns at 101 km (LIN-A; RMS = 0.4768), 108 km  
12  
13 567 (LIN-B; RMS = 0.5490) and 126 km (PNL-L; RMS = 0.8107) (Figures 10g, h, i). The top  
14  
15 568 values are consistent with the geophysical evidence for the ~60 km lithosphere-asthenosphere  
16  
17 569 boundary in the SSRZ (Della Vedova et al., 1995; Civile et al., 2008). The bottom of the melting  
18  
19 570 column for both LIN-A and LIN-B lie at or slightly below of the intersection of the 1435°C  
20  
21 571 mantle adiabat and the dry peridotite solidus (~106 km; depths calculated assuming densities of  
22  
23 572 2700 kg m<sup>-3</sup> for the [20 km thick] crust and 3300 kg m<sup>-3</sup> for the mantle). The bottom of the  
24  
25 573 melting column for PNL-L lies between the peridotite solidus and the intersection of the 1435°C  
26  
27 574 adiabat with the G2 pyroxenite solidus (~137 km; Pertermann and Hirschmann, 2003). It is  
28  
29 575 important to note that the results of these models are relative rather than absolute—for instance,  
30  
31 576 if the garnet-spinel transition zone is fixed at 75-95 km for a mantle potential temperature of  
32  
33 577 1450°C, identical results are obtained for a top and bottom 3 km deeper (viz., 62-63 km top and  
34  
35 578 104-124 km bottom), although the intersections of the adiabats with the solidi would be 4-6 km  
36  
37 579 deeper (dry peridotite: 112 km, pyroxenite: 141 km).

38  
39 580 These results suggest that the Linosa basalts are produced by variable degrees of partial  
40  
41 581 melting (~2% for LIN-A and ~5% for LIN-B) of similar peridotitic asthenosphere. The presence  
42  
43 582 in each diagram of a small, low-fraction melt “tail” at the base of the melting column may flag  
44  
45 583 the presence of a minor amount of lithologically enriched and possibly water-rich material  
46  
47 584 (Gibson and Geist, 2010). This “tail” is deeper, much larger, and more prominent in the PNL-L  
48  
49 585 melting curve, which supports the hypothesis that the mantle source beneath Pantelleria is much  
50  
51  
52  
53  
54  
55  
56  
57  
58  
59  
60  
61  
62  
63  
64  
65

1  
2  
3  
4 586 more enriched in incompatible trace elements. Likewise, the predicted melting column extends  
5  
6  
7 587 below the peridotite solidus to 126 km at  $T_p = 1435^\circ\text{C}$ , consistent with early melting of  
8  
9 588 pyroxenitic material, which is more fusible than peridotite and under these conditions would  
10  
11  
12 589 begin melting between 115-130 km (Hirschmann and Stolper, 1996; Kogiso et al., 1998;  
13  
14 590 Pertermann and Hirschmann, 2003). The model for PNL-L also suggests a fraction of partial  
15  
16 591 melting similar to LIN-B (~5.5%). The INVMEL model was applied to Pantelleria basalts by  
17  
18  
19 592 Neave et al. (2012), who reported similar results (melting across 100-60 km with the garnet-  
20  
21 593 spinel transition zone between 90-70 km, corresponding to a mantle potential temperature of  
22  
23  
24 594 ~1400°C) but with a much lower melt fraction (~1.7%). This lower value is likely due to the  
25  
26 595 inclusion of high-La/Yb PNL-H samples with the PNL-L basalts and their use of a primitive  
27  
28  
29 596 mantle source in their model.  
30

## 31 597

### 32 598 **5.0 Summary**

33  
34  
35  
36 599 Geochemical modelling of basaltic magmatism supports previous geophysical models for  
37  
38 600 the structure of the lithosphere in the Strait of Sicily, suggesting the lithosphere-asthenosphere  
39  
40  
41 601 boundary beneath the islands occurs at ~60 km, with the Moho beneath Linosa at ~24-25 km and  
42  
43 602 high-level magma reservoirs occurring at the top of the crystalline basement between 4 and 8 km.  
44  
45  
46 603 Basalts on both islands fractionated in high-level chambers, although the more primitive magmas  
47  
48 604 erupted on Linosa fractionated from chambers emplaced at the Moho. The asthenosphere  
49  
50  
51 605 underneath the SSRZ is characterized by mantle potential temperatures of 1415-1435°C and  
52  
53 606 consists of depleted MORB lherzolite well-mixed with recycled MORB lithosphere (as  
54  
55 607 eclogite/garnet pyroxenite), in agreement with Avanzinelli et al. (2014). For the most primitive  
56  
57  
58 608 basalts on Linosa (termed LIN-A and primarily represented by the younger [530 ka] Monte  
59  
60  
61  
62  
63  
64  
65

1  
2  
3  
4 609 Bandiera volcanics), there is good agreement between major-element models (FRACTIONATE-  
5  
6  
7 610 PT3; Lee et al., 2009), thermodynamic models of isentropic mantle melting (pMELTS; Ghiorso  
8  
9 611 et al., 2002), and trace element inversion models (INVMEL; McKenzie and O’Nions, 1991,  
10  
11 612 1995). The models collectively suggest that these basalts are the result of ~2% partial melting of  
12  
13  
14 613 a mantle source dominated by depleted MORB mantle (DMM) lithologically enriched with a  
15  
16 614 relatively small fraction of recycled MORB (as eclogite/garnet pyroxenite). The older, generally  
17  
18  
19 615 more evolved basalts on Linosa (termed LIN-B and primarily represented by the older [700 ka]  
20  
21 616 Arena Bianca volcanics) formed from a higher degree of partial melting (~5%) of the same  
22  
23  
24 617 mantle source. In comparison with Linosa, the geochemistry of the basalts on Pantelleria  
25  
26 618 provide evidence that they were sourced from DMM-dominated mantle lithologically enriched  
27  
28  
29 619 with a much larger fraction of recycled MORB and possibly other components; evidence for this  
30  
31 620 includes higher TiO<sub>2</sub> and P<sub>2</sub>O<sub>5</sub> at a given MgO compared to Linosa, higher Sm/Yb and Dy/Yb at  
32  
33 621 a given La/Yb coupled with a lower Zr/Yb, and higher Rb/La coupled with higher <sup>206</sup>Pb/<sup>204</sup>Pb  
34  
35  
36 622 ratios (cf. Avanzineli et al., 2004). The results of INVMEL modelling also indicate that the  
37  
38 623 Pantelleria basalts cannot be derived from a peridotite-only source. We hypothesize that greater  
39  
40  
41 624 melt productivity at Pantelleria and its ability to drive felsic magmatism compared to the  
42  
43 625 remainder of the SSRZ may simply be due to the presence of more fusible mantle beneath the  
44  
45  
46 626 island, indicating mantle heterogeneity at a relatively short length-scale in the SSRZ.  
47

## 48 627 49 50 628 **Acknowledgements**

51  
52  
53 629 The authors thank editor Catherine Chauvel and two anonymous reviewers for their helpful  
54  
55 630 reviews of this paper. Earlier versions of this manuscript were reviewed by Ray Macdonald,  
56  
57  
58 631 Silvio Mollo, and an anonymous reviewer whose comments improved it greatly. JCW would  
59  
60  
61  
62  
63  
64  
65

1  
2  
3  
4  
5  
6  
7  
8  
9  
10  
11  
12  
13  
14  
15  
16  
17  
18  
19  
20  
21  
22  
23  
24  
25  
26  
27  
28  
29  
30  
31  
32  
33  
34  
35  
36  
37  
38  
39  
40  
41  
42  
43  
44  
45  
46  
47  
48  
49  
50  
51  
52  
53  
54  
55  
56  
57  
58  
59  
60  
61  
62  
63  
64  
65

632 also like to thank Mitchell May and Cassie Simpson for their assistance in the field and computer  
633 lab, respectively. This study was funded in part by a grant to JCW from the University Research  
634 Committee and the Rowlett Award from the Society of Foundation Professors at Eastern  
635 Kentucky University. DAN was supported by a Presidential Fellowship from the University of  
636 Manchester

637

638 **References**

639 Aissi, M., Flovere, M., Würtz, M., 2015. Seamounts and seamount-like structures of Sardinia  
640 Channel, Strait of Sicily, Ionian Sea, and Adriatic Sea. In: Würtz, M., Rovere, M.  
641 (Editors), Atlas of the Mediterranean Seamounts and Seamount-like Structures.  
642 International Union for Conservation of Nature (IUCN), Gland, Switzerland and Málaga,  
643 Spain, 187-225, doi: 10.2305/ICUN.CH.2015.07.en

644 Argnani, A., Torelli, L., 2001. The Pelagian Shelf and its graben system (Italy/Tunisia). In:  
645 Ziegler, P.A., Cavazza, W., Robertson, A.H.F. and Crasquin-Soleau, S. (Editors), Peri-  
646 Tethys Memoir 6: Peri-Tethyan Rift/Wrench Basins and Passive Margins. Mém. Mus.  
647 Natl. Hist. Nat. 186, 529-544.

648 Arevalo, R., Jr., McDonough, W.F., Luong, M., 2009. The K/U ratio of the silicate Earth:  
649 Insights into mantle composition, structure, and thermal evolution. Earth Planet. Sci. Lett.  
650 278, 361-369, doi: 1016/j.espl.2008.12.023.

651 Asimow, P.D., Ghiorso, M.S., 1998. Algorithmic modifications extending MELTS to calculated  
652 subsolidus phase relations. Amer. Miner. 83, 1127-1131, doi: 10.2138/am-1998-9-1022.

1  
2  
3  
4  
5  
6  
7  
8  
9  
10  
11  
12  
13  
14  
15  
16  
17  
18  
19  
20  
21  
22  
23  
24  
25  
26  
27  
28  
29  
30  
31  
32  
33  
34  
35  
36  
37  
38  
39  
40  
41  
42  
43  
44  
45  
46  
47  
48  
49  
50  
51  
52  
53  
54  
55  
56  
57  
58  
59  
60  
61  
62  
63  
64  
65

653 Avanzinelli, R., Bindi, L., Menchetti, S., Conticelli, S., 2004. Crystallization and genesis of  
654 peralkaline magmas from Pantelleria Volcano, Italy: An integrated petrological and  
655 crystal-chemical study. *Lithos* 73, 41-69, doi: 10.1016/j.lithos.2013.10.008.

656 Avanzinelli, R., Braschi, E., Marchionni, S., Bindi, L., 2014. Mantle melting in within-plate  
657 continental settings: Sr-Nd-Pb and U-series isotope constraints in alkali basalts from the  
658 Sicily Channel (Pantelleria and Linosa Islands, Southern Italy). *Lithos* 188, 113-129. doi:  
659 10.1016/j.lithos.2013.008.

660 Beccaluva, L., Colantoni, P., Di Girolamo, P., Savelli, C., 1981. Upper-Miocene submarine  
661 volcanism in the Strait of Sicily (Banco senza Nome). *Bull. Volcanol.* 44, 573-581, doi:  
662 10.1007/BF02600587.

663 Bellani, S., Calore, C., Grassi, S., Squarci, P., 1995. Thermal prospecting in Pantelleria island  
664 (Sicily Channel, Italy). *World Geothermal Congress, Firenze 1995*, 2, 767-770, doi:  
665 10.13140/RG.2.1.1040.0165.

666 Berrino, G., Capuano, P., 1995. Gravity anomalies and structures at the island of Pantelleria.  
667 *Acta Vulcanol.* 7, 19-26.

668 Bindi, L., Tasselli, F., Olmi, F., Peccerillo, A., Menchetti, S., 2002. Crystal chemistry of  
669 clinopyroxenes from Linosa Volcano, Sicily Channel, Italy: implications for modelling  
670 the magmatic plumbing system. *Mineral. Mag.* 66, 953-968, doi:  
671 10.1180/0026461026660070.

672 Calanchi, N., Colantoni, P., Rossi, P.L., Saitta, M., Serri, G., 1989. The Strait of Sicily  
673 continental rift systems: Physiography and petrochemistry of the submarine volcanic  
674 centers. *Marine Geol.* 87, 55-83, doi: 10.1016/0025-3227(89)90145-X.

1  
2  
3  
4  
5  
6  
7  
8  
9  
10  
11  
12  
13  
14  
15  
16  
17  
18  
19  
20  
21  
22  
23  
24  
25  
26  
27  
28  
29  
30  
31  
32  
33  
34  
35  
36  
37  
38  
39  
40  
41  
42  
43  
44  
45  
46  
47  
48  
49  
50  
51  
52  
53  
54  
55  
56  
57  
58  
59  
60  
61  
62  
63  
64  
65

675 Catalano, S., De Guidi, G., Lanzafame, G., Monaco, C., Tortorici, L., 2009. Late Quaternary  
676 deformation on the island of Pantelleria: New constraints for the recent tectonic evolution  
677 of the Sicily Channel Rift (southern Italy). *J. Geodyn.* 48, 75-82, doi:  
678 10.1016/j.jog.2009.06.005.

679 Cavallaro, D., Coltelli, M., 2019. The Graham Volcanic Field offshore southwestern Sicily  
680 (Italy) revealed by high-resolution seafloor mapping and ROV images. *Front. Earth Sci.*  
681 7: 311, doi: 10.3389/feart.2019.00311.

682 Civetta, L., D'Antonio, M., Orsi, G., Tilton, G.R., 1998. The geochemistry of volcanic rocks  
683 from Pantelleria Island, Sicily Channel: Petrogenesis and characteristics of the mantle  
684 source region. *J. Petrol.* 39, 1453-1491, doi: 10.1093/petrology/39.8.1453.

685 Civile, D., Lodolo, E., Tortorici, L., Lanzafame, G., Brancolini, G., 2008. Relationships between  
686 magmatism and tectonics in a continental rift: The Pantelleria Island region (Sicily  
687 Channel, Italy). *Marine Geol.* 251, 32-46, doi: 10.1016/j.margeo.2008.01.009.

688 Class, C., Goldstein, S.L., 2005. Evolution of helium isotopes in the Earth's mantle. *Nature* 436,  
689 1107-1112, doi: 10.1038/nature03930.

690 Coltelli, M., Cavallaro, D., D'Anna, G., D'Alessandro, A., Grassa, F., Mangano, G., Patanè, D.,  
691 Gresta, S., 2016. Exploring the submarine Graham Bank in the Sicily Channel. *Ann.*  
692 *Geophys.* 59(2), S0208, doi: 10.4401/ag-6929.

693 Conte, A.M., Martorelli, E., Calarco, M., Sposato, A., Perinelli, C., Coltelli, M., Chiocci, F.L.,  
694 2014. The 1891 submarine eruption offshore Pantelleria Island (Sicily Channel, Italy):  
695 Identification of the vent and characterization of products and eruptive style. *Geochem.*  
696 *Geophys. Geosyst.* 15, 2555-2574, doi: 10.1002/2014GC005238.

1  
2  
3  
4  
5  
6  
7  
8  
9  
10  
11  
12  
13  
14  
15  
16  
17  
18  
19  
20  
21  
22  
23  
24  
25  
26  
27  
28  
29  
30  
31  
32  
33  
34  
35  
36  
37  
38  
39  
40  
41  
42  
43  
44  
45  
46  
47  
48  
49  
50  
51  
52  
53  
54  
55  
56  
57  
58  
59  
60  
61  
62  
63  
64  
65

697 Cottrell, E., Kelley, K.A., 2013. Redox heterogeneity in Mid-Ocean Ridge Basalts as a function  
698 of mantle source. *Science* 340, 1314-1317, doi: 10.1126/science.1233299.

699 Dasgupta, R., Jackson, M.G., Lee, C.-T.A., 2010. Major element chemistry of ocean island  
700 basalts – Conditions of mantle melting and heterogeneity of mantle source. *Earth Planet.*  
701 *Sci. Lett.* 289, 377-392, doi: 10.1016/j.espl.2009.11.027.

702 Davidson, J., Turner, S., Plank, T., 2013. Dy/Dy\*: Variations arising from mantle sources and  
703 petrogenetic processes. *J. Petrol.* 54, 525-537, doi: 10.1093/petrology/egs076.

704 Davis, F.A., Humayun, M., Hirschmann, M.M., Cooper, R.S., 2013. Experimentally determined  
705 mineral/melt partitioning of first-row transition elements (FRTE) during partial melting  
706 of peridotite at 3 GPa. *Geochim. Cosmochim. Acta* 104, 232-260, doi:  
707 10.1016/j.gca.2012.11.009.

708 Della Vedova, B., Lucazeau, F., Pasquale, V., Pellis, G., Verdoya, M., 1995. Heat flow in the  
709 tectonic provinces crossed by the southern segment of the European Geotraverse.  
710 *Tectonophysics* 244, 57-74, doi: 10.106/0040-1951(94)00217-W.

711 Di Bella, M., Russo, S., Petrelli, M., Peccerillo, A., 2008. Origin and evolution of the Pleistocene  
712 magmatism of Linosa Island (Sicily Channel, Italy). *Eur. J. Mineral.* 20: 587-601, doi:  
713 10.1127/0935-1221/2008/0020-1832.

714 Esperança, S., Crisci, G.M., 1995. The island of Pantelleria: A case for the development of  
715 DMM-HIMU isotopic compositions in a long-lived extensional setting. *Earth Planet. Sci.*  
716 *Lett.* 136, 167-182, doi: 10.1016/0012-821X(95)00178-F.

717 Fouré, E., Allard, P., Jean-Baptiste, P., Cellura, D., Parello, F., 2012.  $^3\text{He}/^4\text{He}$  ratio in olivines  
718 from Linosa, Ustica, and Pantelleria Islands (Southern Italy). *J. Geol. Res.*, doi:  
719 10.1155/2012/723839.

1  
2  
3  
4  
5  
6  
7  
8  
9  
10  
11  
12  
13  
14  
15  
16  
17  
18  
19  
20  
21  
22  
23  
24  
25  
26  
27  
28  
29  
30  
31  
32  
33  
34  
35  
36  
37  
38  
39  
40  
41  
42  
43  
44  
45  
46  
47  
48  
49  
50  
51  
52  
53  
54  
55  
56  
57  
58  
59  
60  
61  
62  
63  
64  
65

720 Fulignati, P., Malfitano, G., Sbrana, A., 1997. The Pantelleria caldera geothermal system: Data  
721 from the hydrothermal minerals. *J. Volcanol. Geotherm. Res.* 75, 251-270, doi:  
722 10.1016/S0377-0273(96)00066-2.

723 Gemmellaro, C., 1831. Relazione dei fenomeni del nuovo vulcano sorto dal mare fra la costa di  
724 Sicilia e l'isola di Pantelleria nel mese di luglio 1831. *Atti dell'Accademia Gioenia di*  
725 *Scienze Naturali in Catania* 8, 271-298.

726 Ghiorso, M.S., Sack, R.O., 1995. Chemical mass transfer in magmatic processes. IV. A revised  
727 and internally consistent thermodynamic model for the interpolation and extrapolation of  
728 liquid-solid equilibria in magmatic systems at elevated temperatures and pressures.  
729 *Contrib. Mineral. Petrol.* 119, 197-212, doi: 10.1007/BF00307281.

730 Ghiorso, M.S., Hirschmann, M.M., Reiners, P.W., Kress, V.C., 2002. The pMELTS: A revision  
731 of MELTS aimed at improving calculation of phase relations and major element  
732 partitioning involved in partial melting of the mantle at pressures up to 3 Gpa. *Geochem.*  
733 *Geophys.* 3(5), doi: 10.1029/2001GC000217.

734 Gibson, S.A., Geist, D., 2010. Geochemical and geophysical estimates of lithospheric thickness  
735 variation beneath Galápagos. *Earth Planet. Sci. Lett.* 300, 275-286, doi:  
736 10.1016/j.epsl.2010.10.002.

737 Gualda, G.A.R., Ghiorso, M.S., Lemons, R.V., Carley, T.L., 2012. Rhyolite-MELTS: a modified  
738 calibration of MELTS optimized for silica-rich, fluid-bearing magmatic systems. *J.*  
739 *Petrol.* 53, 875-890, doi: 10.1093/petrology/egr080.

740 Haggerty, S.E., Fung, A.T., Burt, D.M., 1994. Apatite, phosphorous and titanium in eclogitic  
741 garnet from the upper mantle. *Geophys. Res. Lett.* 21, 1699-1702, doi:  
742 10.1029/94GL01001.



1  
2  
3  
4  
5  
6  
7  
8  
9  
10  
11  
12  
13  
14  
15  
16  
17  
18  
19  
20  
21  
22  
23  
24  
25  
26  
27  
28  
29  
30  
31  
32  
33  
34  
35  
36  
37  
38  
39  
40  
41  
42  
43  
44  
45  
46  
47  
48  
49  
50  
51  
52  
53  
54  
55  
56  
57  
58  
59  
60  
61  
62  
63  
64  
65

743 Halliday, A.N., Lee, D.-C., Tommasini, S., Davies, G.R., Paslick, C.R., Fitton, J.G., James, D.E.,  
744 1995. Incompatible trace elements in OIB and MORB and source enrichment in the sub-  
745 oceanic mangle. *Earth Planet. Sci. Lett.* 113, 379-395, doi: 10.1016/0012-  
746 821X(95)00097-V.

747 Herzberg, C., Asimow, P.D., 2008. PRIMELT3 MEGA.XLSM software for primary magma  
748 calculation: Peridotite primary magma MgO contents from the liquidus to the solidus.  
749 *Geochem. Geophys.* 16, 563-578, doi: 10.1002/2014GC00563.

750 Hirschmann, M.M., Stolper, E.M., 1996. A possible role for garnet pyroxenite in the origin of the  
751 “garnet signature” in MORB. *Contrib. Mineral. Petrol.* 124, 185-208, doi:  
752 10.1007/s004100050184.

753 Hofmann, A.W., Jochum, K.P., Seufert, M., White, W.M., 1986. Nb and Pb in oceanic basalts:  
754 new constraints on mantle evolution. *Earth Planet. Sci. Lett.* 79, 33-45, doi:  
755 10.1016/0012-821X(86)90038-5.

756 Irvine, T.N., Baragar, W.R.A., 1971. A guide to the chemical classification of the common  
757 volcanic rocks. *Can. J. Earth Sci.* 8, 523-548, doi: 10.1139/e71-055.

758 Jackson, M.G., Dasgupta, R., 2008. Compositions of HIMU, EM1, and EM2 from global trends  
759 between radiogenic isotopes and major elements in oceanic island basalts. *Earth Planet.*  
760 *Sci. Lett.* 276, 175-186, doi: 10.1016/j.espl.2008.09.023.

761 Katz, R.F., Spiegelman, M., Langmuir, C.H., 2003. A new parameterization of hydrous mantle  
762 melting. *Geochem. Geophys.* 4(9), 1073, doi: 10.1029/2002GC000433.

763 Kelly, J.T., Carey, S., Pistolesi, M., Rosi, M., Croff-Bell, K.L., Roman, C., Marani, M., 2014.  
764 Exploration o the 1891 Foerstner submarine vent site (Pantelleria, Italy): insights into the  
765 formation of basaltic balloons. *Bull. Volc.* 76:844, doi: 10.1007/s00445-014-0844-4.

1  
2  
3  
4  
5  
6  
7  
8  
9  
10  
11  
12  
13  
14  
15  
16  
17  
18  
19  
20  
21  
22  
23  
24  
25  
26  
27  
28  
29  
30  
31  
32  
33  
34  
35  
36  
37  
38  
39  
40  
41  
42  
43  
44  
45  
46  
47  
48  
49  
50  
51  
52  
53  
54  
55  
56  
57  
58  
59  
60  
61  
62  
63  
64  
65

766 Klemme, S., O'Neill, H.StC., 2000. The near-solidus transition from garnet lherzolite to spinel  
767 lherzolite. *Contrib. Mineral. Petrol.* 138, 237-248, doi: 10.1007/s004100050560.

768 Kogiso, T., Hirose, K., Takahashi, E., 1998. Melting experiments on homogenous mixtures of  
769 peridotite and basalt: application to the genesis of ocean island basalts. *Earth Planet. Sci.*  
770 *Lett.* 162, 45-61, doi: 10.1016/S0012-821X(98)00156-3.

771 Langmuir, C.H., Klein, E.M., Plank, T., 1992. Petrological systematics of mid-ocean ridge  
772 basalts: Constraints on melt generation beneath ocean ridges, In: J.P. Morgan, D.K.  
773 Blackman, and J.M. Sinton (Eds.) *Mantle flow and melt generation at mid-ocean ridges,*  
774 *Geophys. Monogr. Ser.* 71, 183-280. AGU, Washington D.C, doi:  
775 10.1029/GM071p0183.

776 Lanzafame, G., Rossi, P.L., Tranne, C.A., Lanti, E., 1994. Carta geologica dell'isola di Linosa.  
777 1:5000. Società Elaborazioni Cartografiche, Firenze.

778 Lee, C.-T.A., Luffi, P., Plank, T., Dalton, H., Leeman, W.P., 2009. Constraints on the depths and  
779 temperatures of basaltic magma generation on Earth and other terrestrial planets using  
780 new thermobarometers for mafic magmas. *Earth Planet. Sci. Lett.* 279, 20-33, doi:  
781 10.1016/j.espl.2008.12.020.

782 Le Maitre, R.W. (Editor), 2002. *Igneous rocks, a classification and glossary of terms:*  
783 *Recommendations of the International Union of Geological Sciences Subcommission on*  
784 *the Systematics of Igneous Rocks, 2<sup>nd</sup> Ed.* Cambridge University Press, 236 p.

785 Lodolo, E., Zampa, L., Civile, D., 2019. The Graham and Terrible volcanic province (NW  
786 Sicilian Channel): gravimetric constraints for the magmatic manifestations. *Bull.*  
787 *Volcanol.* 81, 17, doi:10.1007/s00445-019-1274-0.

1  
2  
3  
4  
5  
6  
7  
8  
9  
10  
11  
12  
13  
14  
15  
16  
17  
18  
19  
20  
21  
22  
23  
24  
25  
26  
27  
28  
29  
30  
31  
32  
33  
34  
35  
36  
37  
38  
39  
40  
41  
42  
43  
44  
45  
46  
47  
48  
49  
50  
51  
52  
53  
54  
55  
56  
57  
58  
59  
60  
61  
62  
63  
64  
65

788 Mahood, G.A., Baker, D.R., 1986. Experimental constraints on depths of fractionation of mildly  
789 alkalic basalts and associated felsic rocks: Pantelleria, Strait of Sicily. *Contrib. Mineral.  
790 Petrol.* 93, 251-264, doi: 10.1007/BF00371327.

791 Mahood, G.A., Hildreth, W., 1986. Geology of the peralkaline volcano at Pantelleria, Strait of  
792 Sicily. *Bull. Volcanol.* 48, 143-172, doi: 10.1007/BF01046548.

793 Martinelli, M., Bistacchi, A., Balsamo, F., Meda, M., 2019. Late Oligocene to Pliocene extension  
794 in the Maltese islands and implications for geodynamics of the Pantelleria Rift and  
795 Pelagian Platform. *Tectonics* 38, 3394-3415, doi: 10.1029/2019TC005627.

796 McDonough, W.F., Sun, S.-s., 1995. The composition of the Earth. *Chem. Geol.* 120, 223-253.

797 McGee, L.E., Smith, I.E.M., Interpreting chemical compositions of small scale basaltic systems:  
798 A review. *J. Volcanol. Geotherm. Res.* 325, 45-60, doi:  
799 10.1016/j.volgeores.2016.06.007.

800 McKenzie, D., Bickle, M.J., 1988. The volume and composition of melt generated by extension  
801 of the lithosphere. *J. Petrol.* 29, 625-679, doi: 10.1093/petrology/29.3.625.

802 McKenzie, D., O’Nions, R.K., 1991. Partial melt distributions from inversion of rare earth  
803 element concentrations. *J. Petrol.* 32, 1021-1091, doi: 10.1093/petrology/32.5.1021.

804 McKenzie, D., O’Nions, R.K., 1995. The source regions of ocean island basalts. *J. Petrol.* 36,  
805 133-159, doi: 10.1093/petrology/36.1.133.

806 McKenzie, D., O’Nions, R.K., 1998. Melt production beneath oceanic islands. *Phys. Earth  
807 Planet. Inter.* 107, 143-182, doi: 10.1016/S0031-9201(97)00132-5.

808 Niu, Y., O’Hara, M.J., 2009. MORB mantle hosts the missing Eu (Sr, Nb, Ta, and Ti) in the  
809 continental crust: New perspectives on crustal growth, crust-mantle differentiation and

1  
2  
3  
4  
5  
6  
7  
8  
9  
10  
11  
12  
13  
14  
15  
16  
17  
18  
19  
20  
21  
22  
23  
24  
25  
26  
27  
28  
29  
30  
31  
32  
33  
34  
35  
36  
37  
38  
39  
40  
41  
42  
43  
44  
45  
46  
47  
48  
49  
50  
51  
52  
53  
54  
55  
56  
57  
58  
59  
60  
61  
62  
63  
64  
65

810 chemical signature of the oceanic upper mantle. *Lithos* 112, 1-17, doi:  
811 10.1016/j.lithos.2008.12.009.

812 Niu, Y., Wilson, M., Humphrey, E.R., and O'Hara, M.J., 2011. The origin of intra-plate ocean  
813 island basalts (OIB): the lid effect and its geodynamic implications. *J. Petrol.* 52, 1443-  
814 1468, doi: 10.1093/petrology/egr030.

815 Neave, D.A., Fabbro, G., Herd, R.A., Petrone, C.M., Edmonds, M., 2012. Melting,  
816 differentiation and degassing at the Pantelleria Volcano, Italy. *J. Petrol.* 53, 637-663, doi:  
817 10.1093/petrology/egr074.

818 O'Hara, M.J., 1968. The bearing of phase equilibria studies in synthetic and natural systems on  
819 the origin and evolution of basic and ultrabasic rocks. *Earth. Sci. Rev.* 4, 69-133, doi:  
820 10.1016/0012-8252(68)90147-5..

821 Parello, F., Allard, P., D'Alessandro, W., Federico, C., Jean-Baptiste, P., Catani, O., 2000.  
822 Isotope geochemistry of Pantelleria volcanic fluids, Sicily Channel rift: a mantle volatile  
823 end-member for volcanism in southern Europe. *Earth Planet. Sci. Lett.* 180, 325-339, doi:  
824 10.1016/S0012-821X(00)00183-7.

825 Parker, D.F., White, J.C., 2008. Large-scale alkalic magmatism associated with the Buckhorn  
826 caldera, Trans-Pecos Texas, USA: Comparison with Pantelleria, Italy. *Bull. Volcanol.*  
827 70, 403-415, doi: 10.1007/s00445-007-0145-2.

828 Pearce, T.H., 1968. A contribution to the theory of variation diagrams. *Contrib. Mineral. Petrol.*  
829 19, 142-157, doi: 10.1007/BF00635485.

830 Pertermann, M., Hirschmann, M.M., 2003. Partial melting experiments on a MORB-like  
831 pyroxenite between 2 and 3 GPa: Constraints on the presence of pyroxenite in basalt

1  
2  
3  
4  
5  
6  
7  
8  
9  
10  
11  
12  
13  
14  
15  
16  
17  
18  
19  
20  
21  
22  
23  
24  
25  
26  
27  
28  
29  
30  
31  
32  
33  
34  
35  
36  
37  
38  
39  
40  
41  
42  
43  
44  
45  
46  
47  
48  
49  
50  
51  
52  
53  
54  
55  
56  
57  
58  
59  
60  
61  
62  
63  
64  
65

832 source retrions from solidus location and melting rate. *J. Geophys. Res.* 108, no. B2, 2125,  
833 doi: 10.1029/2000JB000118.

834 Pertermann, M., Hirschmann, M.M., Hametner, K, Günther, D., Schmidt, M.W., 2004.  
835 Experimental determination of trace element partitioning between garnet and silica-rich  
836 liquid during anhydrous melting of MORB-like eclogite. *Geochem. Geophys.* 5(5),  
837 Q05A01, doi: 10.1029/2003/GC000638.

838 Plank, T., Forsyth, D.W., 2016. Thermal structure and melting conditions in the mantle beneath  
839 the Basin and Range province from seismology and petrology. *Geochem. Geophys.* 17,  
840 1312-1338, doi: 10.1002/2015GC006205.

841 Prytulak, J., Elliot, T., 2007. TiO<sub>2</sub> enrichment in ocean island basalts. *Earth Planet. Sci. Lett.*  
842 263, 388-403, doi: 10.1016/j.epsl.2007.09.015.

843 Putirka, K.D., 2005. Mantle potential temperatures at Hawaii, Iceland, and the mid-ocean ridge  
844 system, as inferred from olivine phenocrysts: Evidence for thermally driven mantle  
845 plumes. *Geochem. Geophys.* 6(5), Q05L08, doi: 10.1029/2005GC000915.

846 Putirka, K.D., Perfit, M., Ryerson, F.J., Jackson, M.G., 2007. Ambient and excess mantle  
847 temperatures, olivine thermometry, and active vs. passive upwelling. *Chem. Geol.* 241,  
848 177-206, doi: 10.1016/j.chemgeo.2007.01.014.

849 Romagnoli, C., Belvisi, V., Innangi, S., Di Martino, G., Tonielli, R., 2020. New insights on the  
850 evolution of the Linosa volcano (Sicily Channel) from the study of its submarine  
851 portions. *Mar. Geol.* 419: 106060, doi: 10.1016/j.margeo.2019.106060.

852 Rossi, P.L., Tranne, C.A., Calanchi, N., Lanti, E., 1996. Geology, stratigraphy and  
853 volcanological evolution of the island of Linosa (Sicily Channel). *Acta Vulcanol.* 8, 73-  
854 90.

1  
2  
3  
4  
5  
6  
7  
8  
9  
10  
11  
12  
13  
14  
15  
16  
17  
18  
19  
20  
21  
22  
23  
24  
25  
26  
27  
28  
29  
30  
31  
32  
33  
34  
35  
36  
37  
38  
39  
40  
41  
42  
43  
44  
45  
46  
47  
48  
49  
50  
51  
52  
53  
54  
55  
56  
57  
58  
59  
60  
61  
62  
63  
64  
65

855 Rotolo, S.G., Castorina, F., Cellura, D., Pompilio, M., 2006. Petrology and geochemistry of  
856 submarine volcanism in the Sicily Channel rift. *J. Geol.* 114, 355-365, doi:  
857 10.1086/501223.

858 Russell, J.K., Nicholls, J., 1988. Analysis of petrologic hypotheses with Pearce element ratios.  
859 *Contrib. Mineral. Petrol.* 99, 25-35, doi: 10.1007/BF00399362.

860 Salters, V.J.M., Stracke, A., 2004. Composition of depleted mantle. *Geochem. Geophys.* 5(5),  
861 Q05004, doi:10.1029/2003GC000597.

862 Scaillet, S., Vita-Scaillet, G., Rotolo, S.G., 2013. Millennial-scale phase relationships between  
863 ice-core and Mediterranean marine records: insights from high-precision  $^{40}\text{Ar}/^{39}\text{Ar}$  dating  
864 of the Green Tuff of Pantelleria, Sicily Strait. *Quat. Sci. Rev.* 78, 141-154, doi:  
865 10.1016/j.quascirev.2013.08.008.

866 Stracke, A., Bourdon, B., 2009. The importance of melt extraction for tracing mantle  
867 heterogeneity. *Geochim. Cosmochim. Acta* 73, 218-238, doi: 10.1016/j.gca.2008.10.015.

868 Stracke, A., 2012. Earth's homogenous mantle: A product of convection-driven interaction  
869 between crust and mantle. *Chem. Geol.* 330-331, 274-299, doi:  
870 10.1016/j.chemgeo.2012.08.007.

871 Sun, S.-s., McDonough, W.F., 1989. Chemical and isotopic systematics of oceanic basalts:  
872 implications for mantle composition and processes. *Geol. Soc. Spec. Pub.* 42, 313-345,  
873 doi: 10.1144/GSL.SP.1989.042.01.19.

874 Tang, M., Rudnick, R.L., McDonough, W.F., Gaschnig, R.M., Huang, Y., 2015. Europium  
875 anomalies constrain the mass of recycled lower continental crust. *Geology* 43, 703-706,  
876 doi: 10.1130/G36641.1.

1  
2  
3  
4  
5  
6  
7  
8  
9  
10  
11  
12  
13  
14  
15  
16  
17  
18  
19  
20  
21  
22  
23  
24  
25  
26  
27  
28  
29  
30  
31  
32  
33  
34  
35  
36  
37  
38  
39  
40  
41  
42  
43  
44  
45  
46  
47  
48  
49  
50  
51  
52  
53  
54  
55  
56  
57  
58  
59  
60  
61  
62  
63  
64  
65

877 Tang, M., McDonough, W.F., Ash, R.D., 2017. Europium and strontium anomalies in the  
878 MORB source mantle. *Geochim. Cosmochim. Acta* 197, 132-141, doi:  
879 10.1016/j.gca.2016.10.025.

880 Tonielli, R., Innangi, S., Di Martino, G., Romagoli, C., 2019. New bathymetry of the Linosa  
881 volcanic complex from multibeam systems (Sicily Channel, Mediterranean Sea). *J. Maps*  
882 15, 611-618, doi: 10.1080/17445647.2019.1642807.

883 van Westrenen, W., Blundy, J.D., Wood, B.J., 2001. High field strength element / rare earth  
884 element fractionation during partial melting in the presence of garnet: Implications for  
885 identification of mantle heterogeneities. *Geochem. Geophys.* 2(7), doi:  
886 10.1029/2000GC000133.

887 Washington, H.S., 1909. Art. VIII.—The submarine eruptions of 1831 and 1891 near Pantelleria.  
888 *Amer. J. Sci.* 27(158), 131-150, doi: 10.2475/ajs.s4-27.158.131.

889 White, R.S., McKenzie, D., O’Nions, R.K., 1992. Oceanic crustal thickness from seismic  
890 measurements and rare earth element inversions. *J. Geophys. Res.* 97, 19683-19715, doi:  
891 10.1029/92JB01749.

892 White, J.C., Parker, D.F., Ren, M., 2009. The origin of trachyte and pantellerite from Pantelleria,  
893 Italy: Insights from major element, trace element, and thermodynamic modelling. *J.*  
894 *Volcanol. Geotherm. Res.* 179, 33-55, doi: 10.1016/j.volgeores.2008.10.007.

895 White, J.C., Espejel-García, V.V., Anthony, E.Y., Omenda, P., 2012. Open system evolution of  
896 peralkaline trachyte and phonolite from the Suswa volcano, Kenya rift. *Lithos* 152, 84-  
897 104, doi: 10.1016/j.lithos.2012.01.023.

898 Wolff, J.A., 2017. On the syenite-trachyte problem. *Geology* 45, 1067-1070, doi:  
899 10.1130/G39415.1.

1  
2  
3  
4  
5  
6  
7  
8  
9  
10  
11  
12  
13  
14  
15  
16  
17  
18  
19  
20  
21  
22  
23  
24  
25  
26  
27  
28  
29  
30  
31  
32  
33  
34  
35  
36  
37  
38  
39  
40  
41  
42  
43  
44  
45  
46  
47  
48  
49  
50  
51  
52  
53  
54  
55  
56  
57  
58  
59  
60  
61  
62  
63  
64  
65

900 Willbold, M., Stracke, A., 2006. Trace element composition of mantle end-members:  
901 Implications for recycling of oceanic and upper and lower continental crust. *Geochem.*  
902 *Geophys.* 7(4), Q04004, doi: 10.1029/2005GC001005.

903 Yang, Z.-F., Zhou, J.-H., 2013. Can we identify source lithology of basalt? *Sci. Rep.* 3, 1856,  
904 doi: 10/1038/srep01856.

905 Zindler, A., Hart, S., 1986. Chemical geodynamics. *Ann. Rev. Earth Planet. Sci.* 14, 493-571,  
906 doi: 10.1146/annurev.ea.14.050186.002425.



1  
2  
3  
4  
5  
6  
7  
8  
9  
10  
11  
12  
13  
14  
15  
16  
17  
18  
19  
20  
21  
22  
23  
24  
25  
26  
27  
28  
29  
30  
31  
32  
33  
34  
35  
36  
37  
38  
39  
40  
41  
42  
43  
44  
45  
46  
47  
48  
49  
50  
51  
52  
53  
54  
55  
56  
57  
58  
59  
60  
61  
62  
63  
64  
65

907 **FIGURE CAPTIONS**

908  
909 Figure 1. Location of the Strait of Sicily, Italy-Tunisia. Rift valleys: PT, Pantelleria Trough; LT,  
910 Linosa Trough; MT, Malta Trough. Volcanic seamounts (Aissi et al., 2015): A, Anfitrite; AN,  
911 Angelina; C, Cimotoc; CB, Pantelleria Central Bank; E, Pantelleria East; F, Foerstner; GB,  
912 Graham Bank; G, Galatea; L1, Linosa I; L2, Linosa II; L3, Linosa III; NB, Nameless Bank; P,  
913 Pinne; SE, Pantelleria Southeast; SW, Pantelleria Southwest. GoogleEarth v.7.3.2.5776 (13  
914 December 2015). 36.7649°N 12.8443°E, Eye alt 520 km. SIO, NOAA, US Navy, GEBCO.  
915 <http://www.earth.google.com> [20 November 2019]

916  
917 Figure 2. (a) Total-alkali versus silica (TAS) diagram for the classification of volcanic rocks (Le  
918 Maitre, 2002). (b) Basalt tetrahedron projected from clinopyroxene:  $Q' = q + 0.4ab + 0.25hy$ ;  $Ol'$   
919  $= ol + 0.75hy$ ;  $Ne' = ne + 0.6ab$  (Irvine and Baragar, 1971). Alkali basalts plot below the plane  
920 of critical silica undersaturation (solid line); transitional basalts plot below the plane of critical  
921 silica saturation (dashed line). Units: PL, Paleo-Linosa; AB, Arena Bianca (Linosa); MB, Monte  
922 Bandiera (Linosa); PP, Paleo-Pantelleria; NP, Neo-Pantelleria; SEA, Semounts.

923  
924 Figure 3. Major-element variation diagrams that use MgO as the differentiation index. Dashed  
925 lines illustrate the two major trends (see text for details.) Units: PL, Paleo-Linosa; AB, Arena  
926 Bianca (Linosa); MB, Monte Bandiera (Linosa); PP, Paleo-Pantelleria; NP, Neo-Pantelleria;  
927 SEA, Seamounts. Trends labeled A and B correspond to the Linosa trends of Di Bella et al.  
928 (2008).

1  
2  
3  
4  
5  
6  
7  
8  
9  
10  
11  
12  
13  
14  
15  
16  
17  
18  
19  
20  
21  
22  
23  
24  
25  
26  
27  
28  
29  
30  
31  
32  
33  
34  
35  
36  
37  
38  
39  
40  
41  
42  
43  
44  
45  
46  
47  
48  
49  
50  
51  
52  
53  
54  
55  
56  
57  
58  
59  
60  
61  
62  
63  
64  
65

930 Figure 4. Trace-element variation diagrams that use MgO as the differentiation index. Units: PL,  
931 Paleo-Linosa; AB, Arena Bianca (Linosa); MB, Monte Bandiera (Linosa); PP, Paleo-Pantelleria;  
932 NP, Neo-Pantelleria; SEA, Seamounts Trends labeled A and B correspond to the Linosa trends  
933 of Di Bella et al. (2008).

934  
935 Figure 5. Representative rare-earth element diagrams (normalized to CI Chondrite; McDonough  
936 and Sun, 1995). In each graph, n = the total number of analyses in the dataset. REE ratios are  
937 reported either as a range or averages with standard deviation.

938  
939 Figure 6. Pearce (1968) element ratios plotted with the results of MELTS (rhyolite-MELTS  
940 v.1.0.2; Gualda et al., 2012) models of fractional crystallization at 0.20 and 0.65 GPa. Vectors  
941 show the slopes of the data distribution trends that would result from the fractionation of olivine  
942 (Ol), clinopyroxene (Cpx), and plagioclase (Pl)

943  
944 Figure 7. FractionatePT3 (Lee et al., 2009) model results for (a) anhydrous and (b) hydrous (1  
945 wt% H<sub>2</sub>O) LIN-A basalts with 10 wt% < MgO < 14 wt% calculated with  $Fe^{3+}/\Sigma Fe = 0.13$  and  
946 mantle Fo = 90 mol%. Plotted with these are the P-T paths for isentropic melting of (a)  
947 anhydrous and (b) hydrous (116 ppm H<sub>2</sub>O) average depleted MORB mantle (DMM; Salters and  
948 Stracke, 2004) calculated with pMELTS (v.5.6.1) at FMQ from the intersections of the 1415°  
949 and 1430° adiabats with the (a) dry and (b) wet (116 ppm H<sub>2</sub>O) lherzolite solidus (Katz et al.,  
950 2003). LAB: lithosphere-asthenosphere boundary. Gt-In, Sp-Out: garnet-spinel transition zone  
951 (Klemme and O'Neill, 2000). Adiabats calculated following McKenzie and Bickle (1988) and  
952 Putirka et al. (2007) (Supplementary Data 1).

1  
2  
3  
4  
5  
6  
7  
8  
9  
10  
11  
12  
13  
14  
15  
16  
17  
18  
19  
20  
21  
22  
23  
24  
25  
26  
27  
28  
29  
30  
31  
32  
33  
34  
35  
36  
37  
38  
39  
40  
41  
42  
43  
44  
45  
46  
47  
48  
49  
50  
51  
52  
53  
54  
55  
56  
57  
58  
59  
60  
61  
62  
63  
64  
65

953

954 Figure 8. Trace element ratio diagrams, with REE ratios normalized to CI Chondrite  
955 (McDonough and Sun, 1995).  $Dy/Dy^* = Dy_N / [La_N^{4/13} \cdot Yb_N^{9/13}]$  (Davidson et al., 2013). Units:  
956 PL, Paleo-Linosa; AB, Arena Bianca (Linosa); MB, Monte Bandiera (Linosa); PP, Paleo-  
957 Pantelleria; NP, Neo-Pantelleria; SEA, Seamounts. Identified geochemical groups are labelled,  
958 as are the interpretations of the variation as discussed in the text.

959

960 Figure 9. Spiderdiagrams of representative samples (normalized to depleted MORB mantle  
961 [DMM]; Salters and Stracke, 2004) for each of the geochemical groups identified in Figure 8.  
962 Values in parenthesis are wt% MgO of each sample. The dotted lines superimposed on each  
963 represent model non-modal fractional melts ( $F = 0.02$ ) of DMM for garnet peridotite (GD) and  
964 spinel peridotite (SD) (see Supplementary Data 2).

965

966 Figure 10. Results of rare-earth element inverse modelling (a, b, c), major- and trace-element  
967 forward model predictions (d, e, f), and calculated melting curves (g, h, j) for LIN-A, LIN-B, and  
968 PNL-L. Chondrite-normalized Sm/Yb values represent the average of the sample set ( $n = \text{total}$   
969 number of samples used in the model). RMS = root mean square error.

Figure 1  
[Click here to download high resolution image](#)

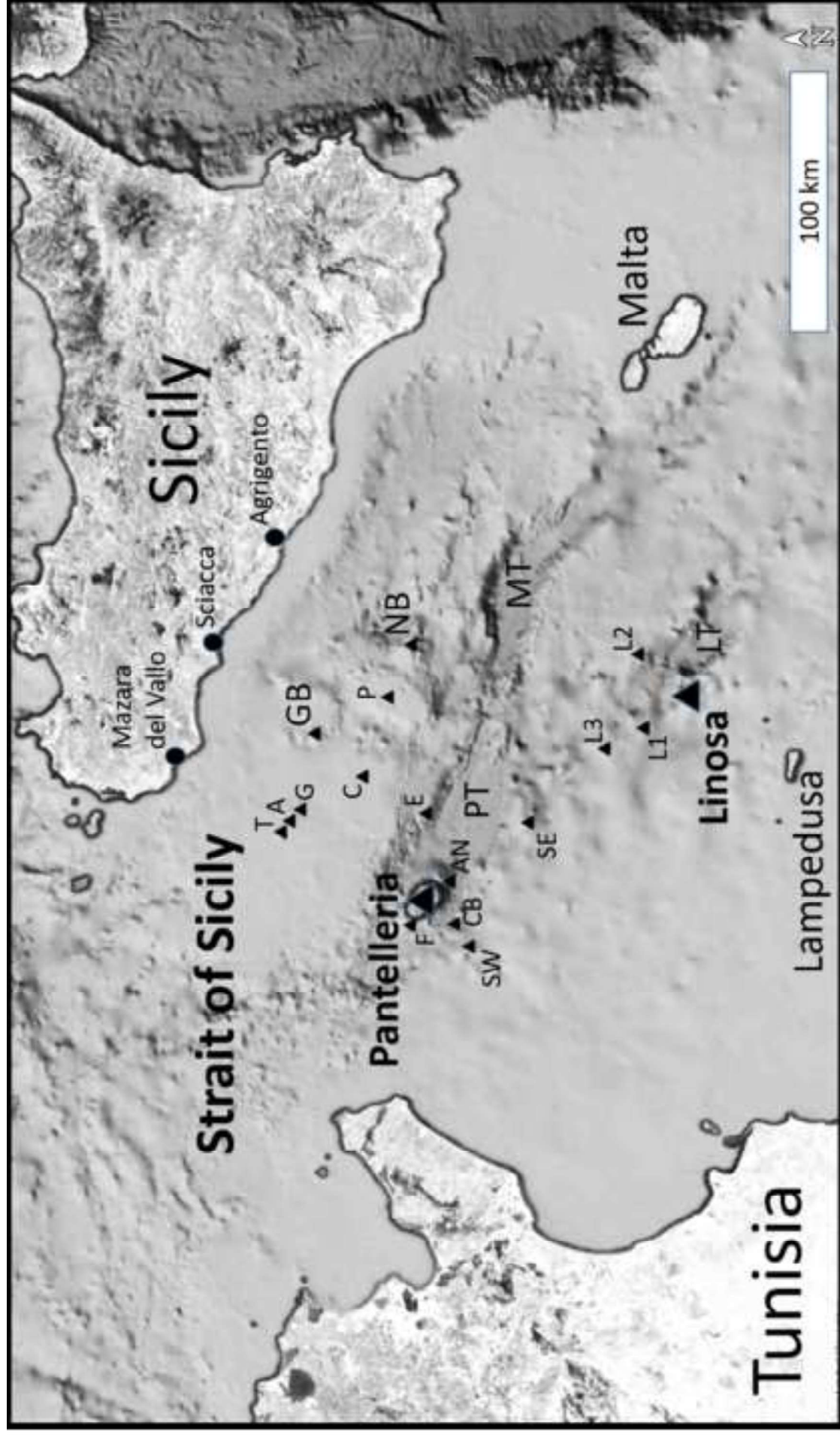


Figure 2

[Click here to download high resolution image](#)

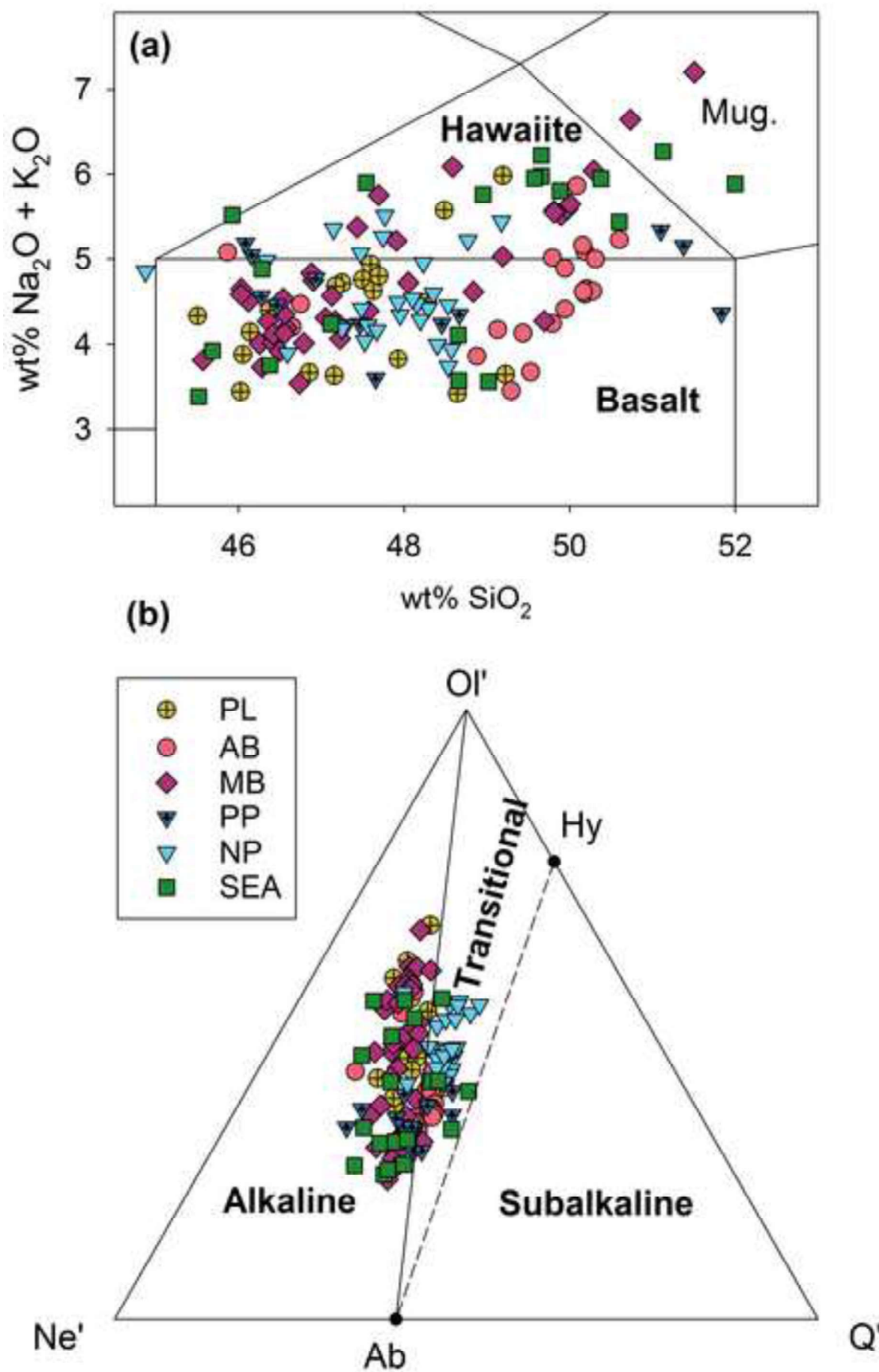


Figure 3  
[Click here to download high resolution image](#)

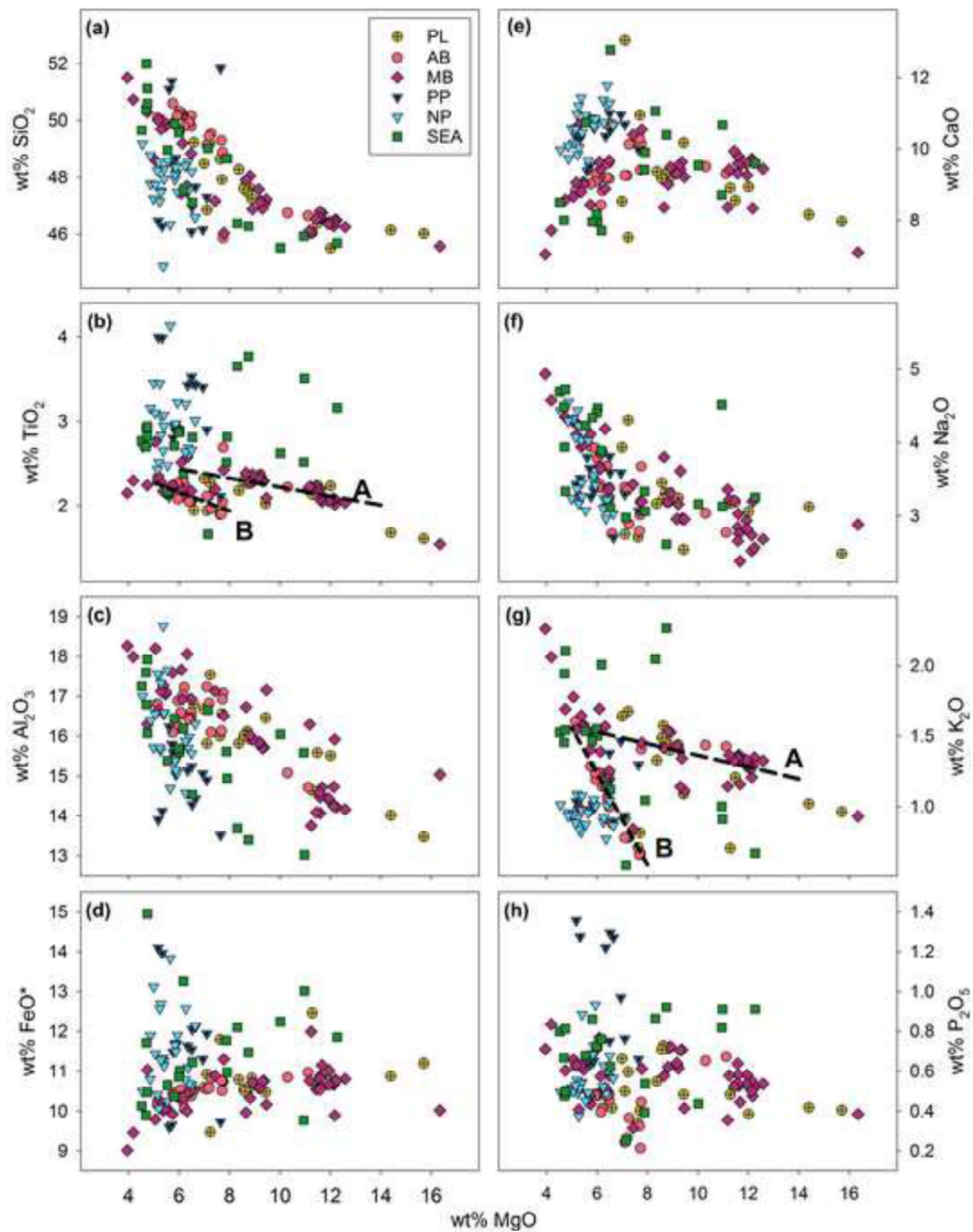


Figure 4  
[Click here to download high resolution image](#)

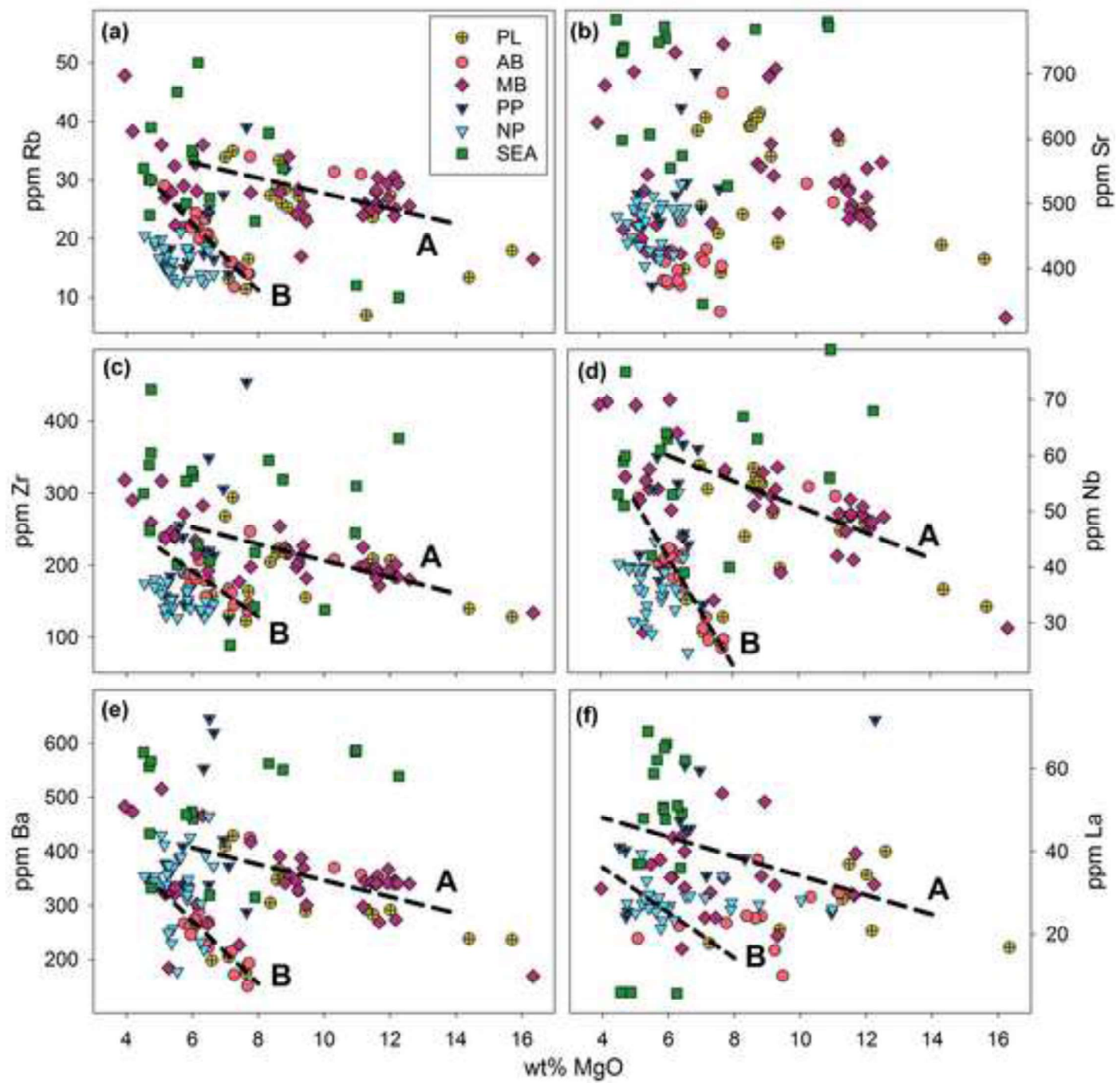


Figure 5

[Click here to download high resolution image](#)

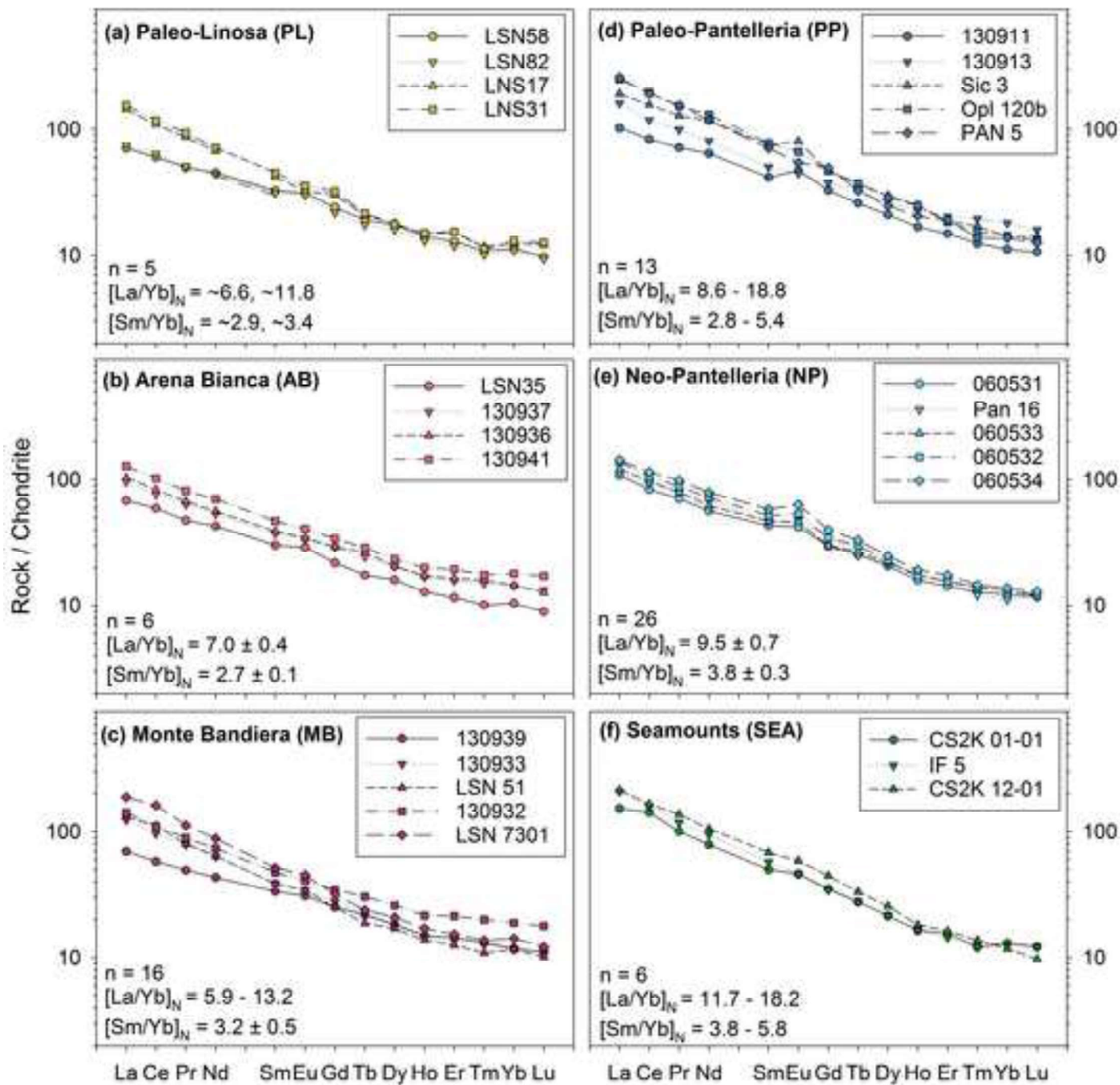




Figure 6  
[Click here to download high resolution image](#)

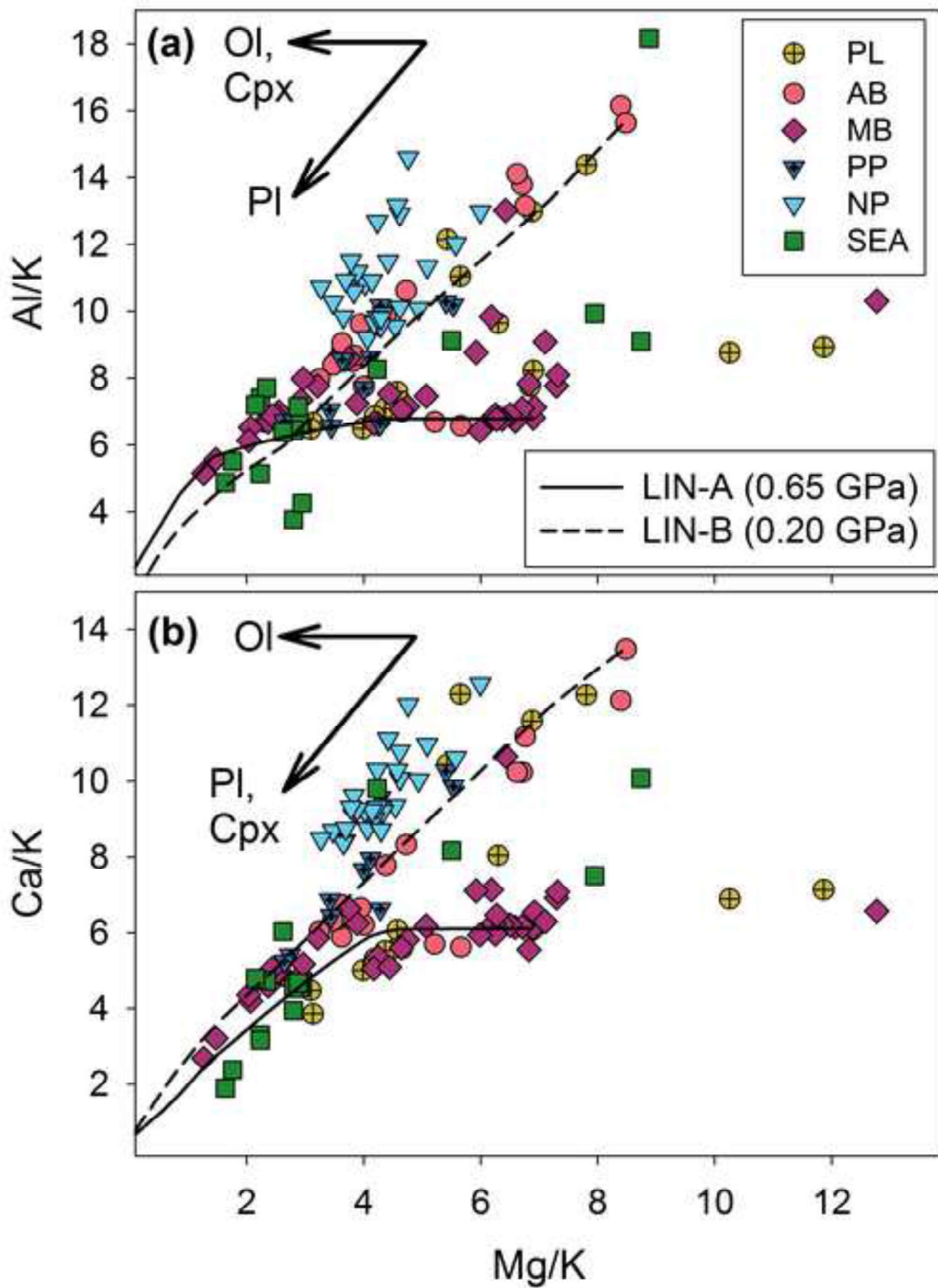


Figure 7  
[Click here to download high resolution image](#)

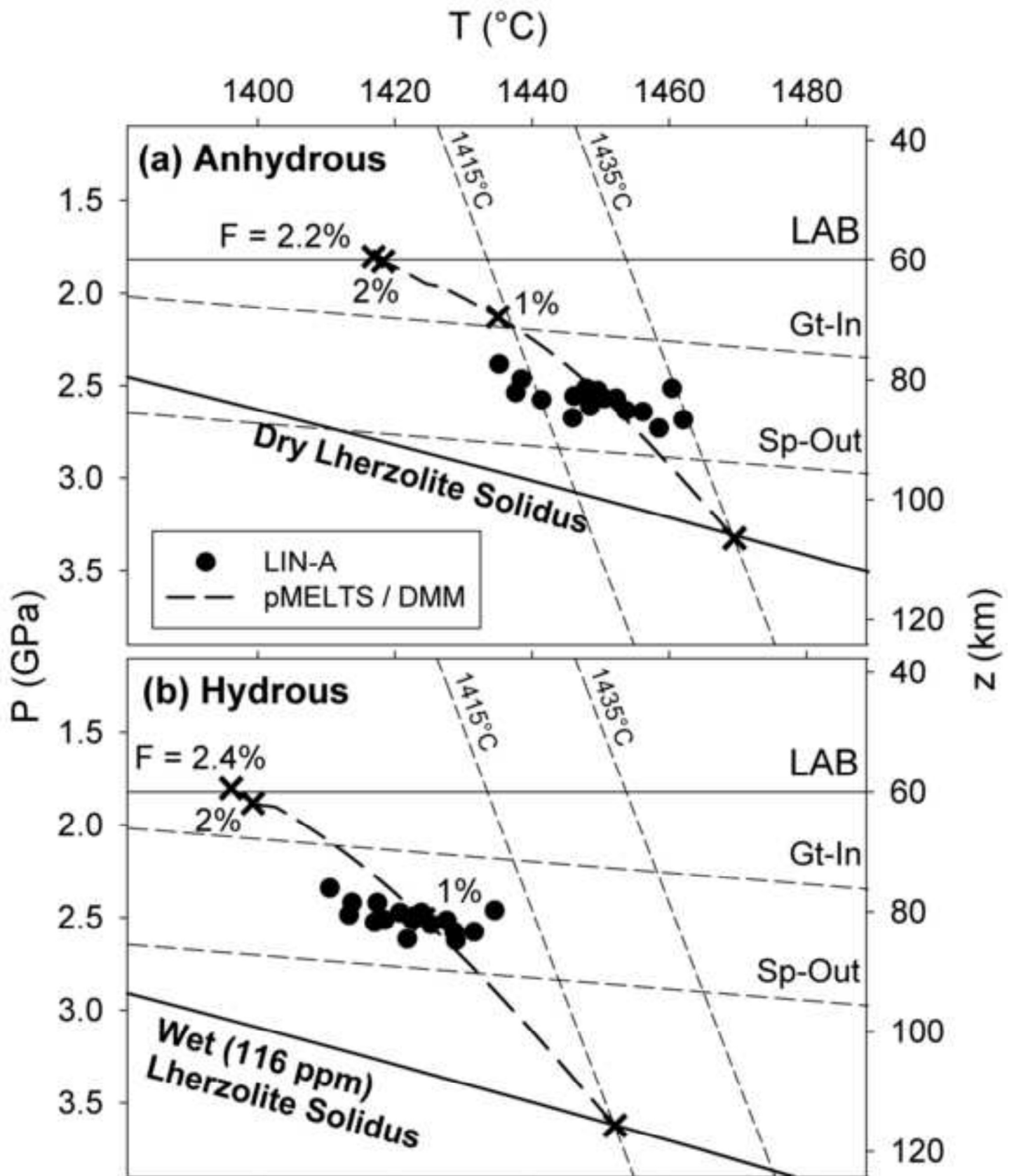


Figure 8  
[Click here to download high resolution image](#)

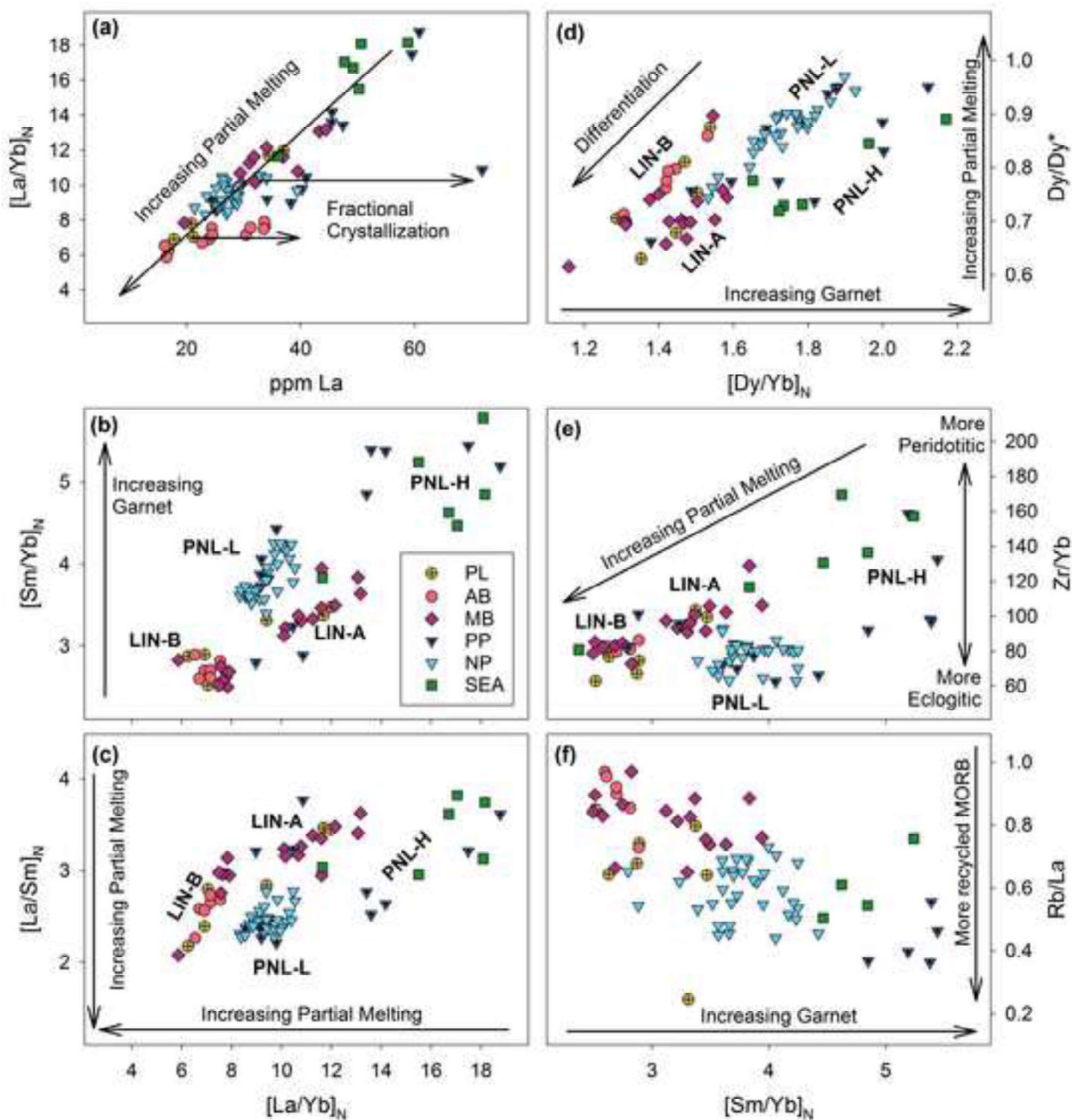
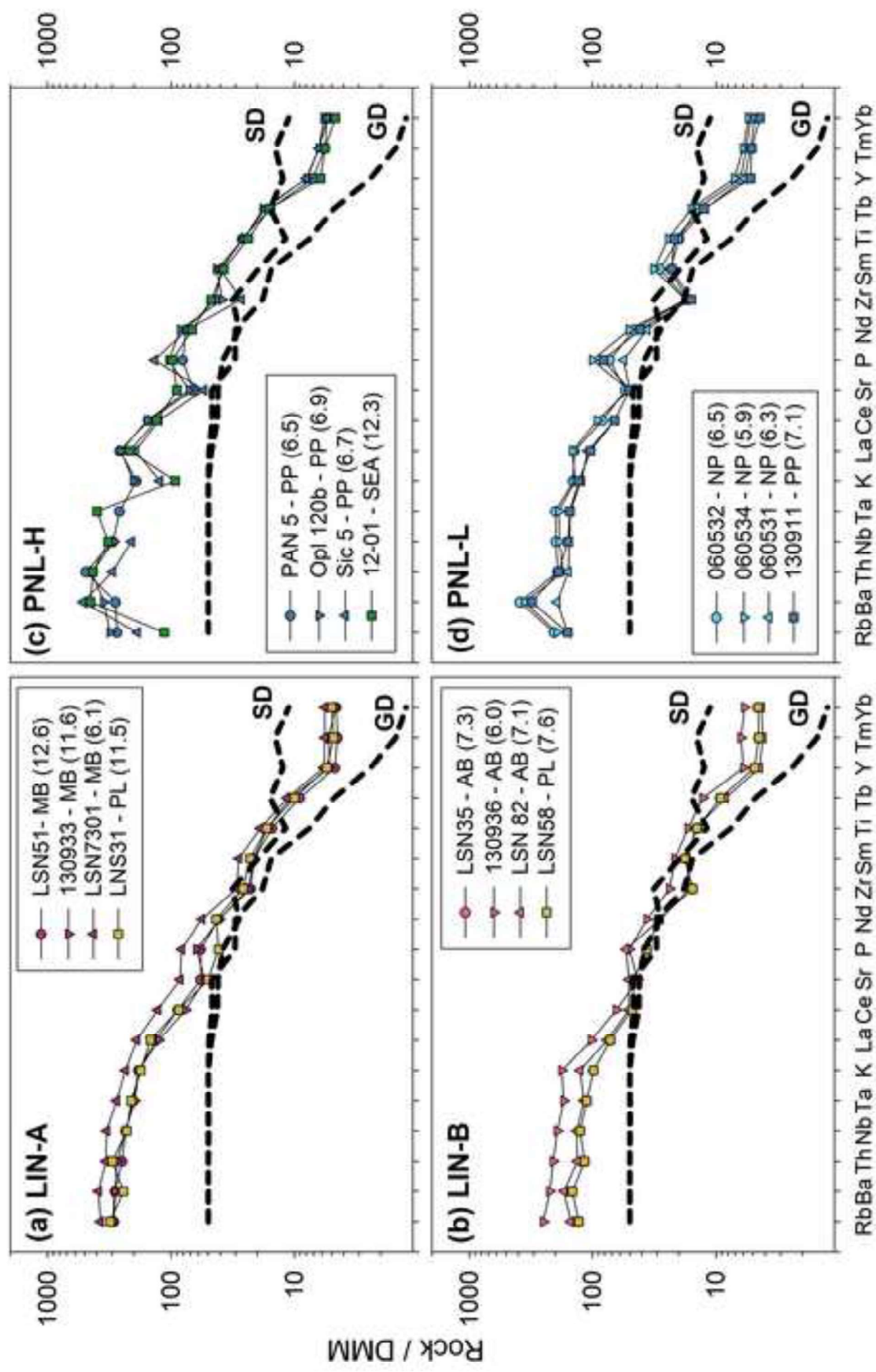


Figure 9

[Click here to download high resolution image](#)



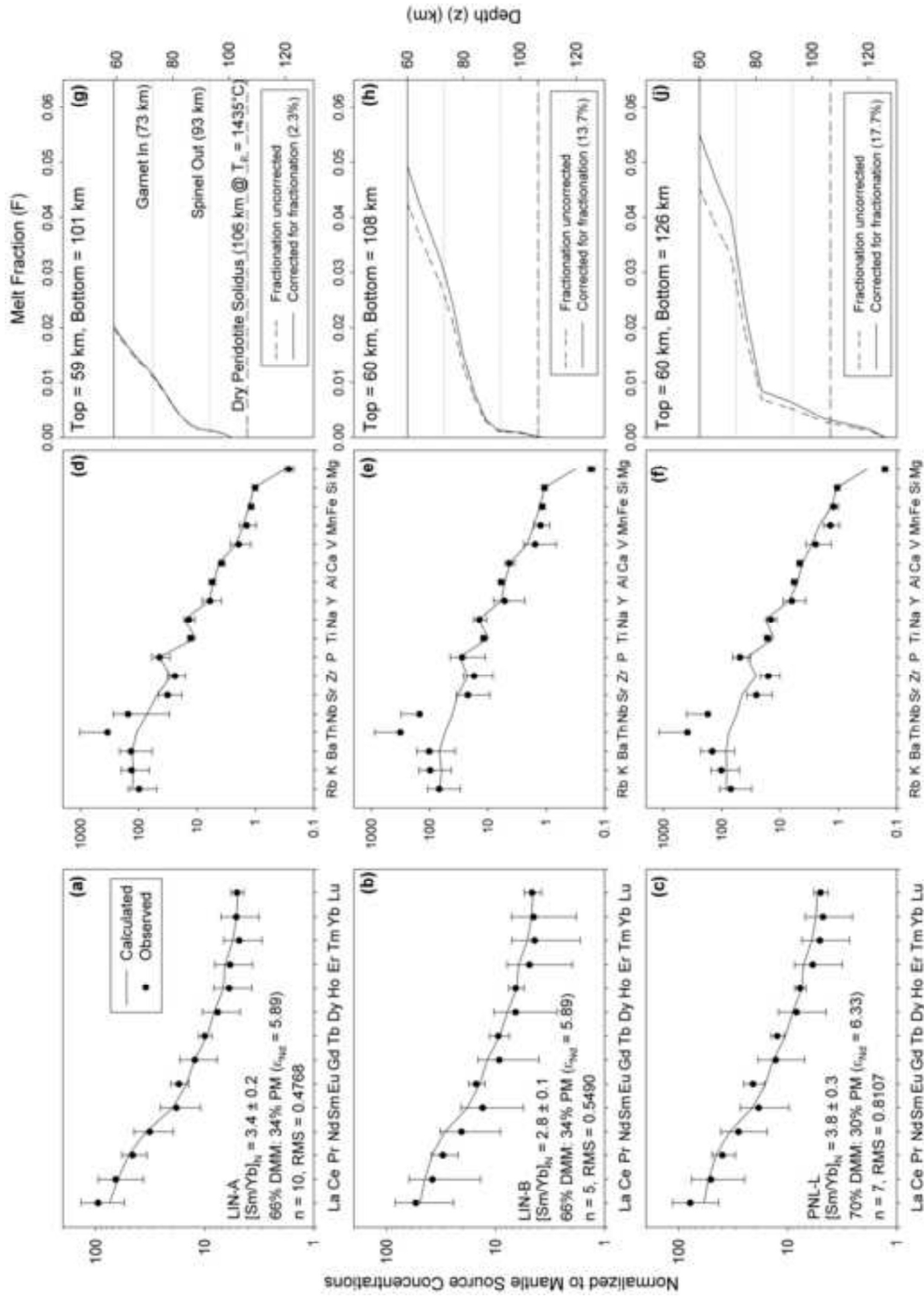


Table 1

[Click here to download Table: Table1.xlsx](#)

Table 1. Major and trace element compositions of volcanic rocks from Pantelleria and Linosa.

Island:	Pantelleria						
Sample ID:	130912	130911	060532	030512	060531	030508	130916
Phase:	PP	PP	NP	NP	NP	NP	PP
Lat (N):	36.8353	36.8107	36.8311	36.8366	36.8269	36.8197	36.8261
Long (E):	11.9691	11.9286	11.9367	11.9477	11.9556	11.9286	11.9364
Class:	tB	aB	aB	tB	aB	AB	aB
SiO <sub>2</sub> , wt%	50.36	47.14	47.72	47.83	48.23	46.52	48.69
TiO <sub>2</sub>	2.05	2.89	2.63	2.65	2.63	3.13	2.88
Al <sub>2</sub> O <sub>3</sub>	13.13	14.85	15.42	15.47	15.82	14.22	15.05
Fe <sub>2</sub> O <sub>3</sub> <sup>T</sup>	10.50	13.22	11.72	12.14	11.94	13.63	12.98
MnO	0.17	0.19	0.17	0.16	0.16	0.18	0.19
MgO	7.43	7.08	6.44	6.27	6.23	6.12	5.87
CaO	9.69	10.65	11.17	11.08	11.33	10.48	10.69
Na <sub>2</sub> O	2.98	3.28	3.21	2.92	3.09	3.16	3.35
K <sub>2</sub> O	1.26	0.93	1.03	0.76	0.89	0.90	1.00
P <sub>2</sub> O <sub>5</sub>	0.64	0.76	0.67	0.48	0.52	0.61	0.65
LOI	0.24	-0.36	0.00	0.00	0.00	0.00	-0.67
Total	98.45	100.63	100.19	99.77	100.84	98.95	100.68
Mg#	60.89	54.09	54.73	53.19	53.44	49.69	49.87
Sc, ppm	22	31	30	32	31	33	32
V	176	307	274	280	295	323	320
Cr	270	90	130	101	120	91	100
Co	37	43	36	64	39	58	38
Ni	170	80	65	57	60	57	50
Cu	20	40	53	n.a.	78	n.a.	40
Zn	130	90	75	94	76	103	100
Ga	22	19	19	17	20	17	21
Ge	1.8	1.7	1.1	1.6	1.1	1.6	2
Rb	39	14	18	12	14	13	16
Sr	523	492	530	485	492	421	472
Y	45.0	21.4	25.6	22.1	23.9	25.3	24.4
Zr	454	126	137	128	136	139	147
Nb	106.0	33.2	41.6	53.5	32.3	36.1	39.4
Ba	288	373	465	219	233	304	335
La	71.80	24.3	32.9	26.0	25.5	28.80	25.6
Ce	136.00	51.3	64.3	49.6	51.3	56.77	54.5
Pr	15.80	6.67	8.24	6.12	6.56	6.98	6.97
Nd	59.20	29.5	32.9	27.4	25.8	31.04	30.4
Sm	11.90	6.17	7.7	6.35	6.37	7.37	6.76
Eu	2.75	2.65	3.02	2.30	2.37	2.74	2.65
Gd	10.80	6.54	6.87	6.39	5.89	7.32	6.59
Tb	1.72	0.94	1.08	1.02	0.92	1.12	1.01
Dy	9.46	5.17	5.61	5.24	5.07	5.91	5.38